The Mid-Infrared Spectrum of the Zodiacal and Exozodiacal Light

William T. Reach and Patrick Morris

SIRTF Science Center/Infrared Processing and Analysis Center, California Institute of Technology, Pasadena, CA 91125

reach@ipac.caltech.edu

François Boulanger

Institut d'Astrophysique Spatiale, 91405 Orsay cedex, France

Koryo Okumura

CEA/DSM/DAPNIA Service d'Astrophysique, F-91191 Gif-sur-Yvette, France

ABSTRACT

The zodiacal light is the dominant source of the mid-infrared sky brightness seen from Earth, and exozodiacal light is the dominant emission from planetary and debris systems around other stars. We observed the zodiacal light spectrum with the mid-infrared camera ISOCAM over the wavelength range 5–16 μm and a wide range of orientations relative to the Sun (solar elongations 68°–113°) and the ecliptic (plane to pole). The temperature in the ecliptic ranged from 269 K at solar elongation 68° to 244 K at 113°, and the polar temperature, characteristic of dust 1 AU from the Sun, is 274 K. The observed temperature is exactly as expected for large ($> 10\mu$m radius), low-albedo (< 0.08), rapidly-rotating, grey particles 1 AU from the Sun. Smaller particles (< 10 μm radius) radiate inefficiently in the infrared and are warmer than observed. We present theoretical models for a wide range of particle size distributions and compositions; it is evident that the zodiacal light is produced by particles in the 10–100 μm radius range. In addition to the continuum, we detect a weak excess in the 9–11 μm range, with an amplitude of 6% of the continuum. The shape of the feature can be matched by a mixture of silicates: amorphous forsterite/olivine provides most of the continuum and some of the 9–11 μm silicate feature, dirty crystalline olivine provides the red wing of the silicate feature (and a bump at 11.35 μm), and a hydrous silicate (montmorillonite) provides the blue wing of the silicate feature. The presence of hydrous silicate suggests the parent bodies of those particles were formed in the inner solar nebula. Large particles dominate the size distribution, but at least some small particles (radii ~ 1 μm) are required to produce the silicate emission feature. The strength of the feature may vary spatially, with the strongest features being at the lowest solar elongations as well as at high ecliptic latitudes; if confirmed, this would imply that the dust properties change such that dust further from the Sun has a weaker silicate feature.

To compare the properties of zodiacal dust to dust around other main sequence stars, we reanalyzed the exozodiacal light spectrum for β Pic to derive the shape of its silicate feature. The zodiacal and exozodiacal spectra are very different. The exozodiacal spectra are dominated by cold dust, with emission peaking in the far-infrared, while the zodiacal spectrum peaks around 20 μm. We removed the debris disk continuum from the spectra by fitting a blackbody with a different temperature for each aperture (ranging from 3.7″ to 27″); the resulting silicate spectra for β Pic are identical for all apertures, indicating that the silicate feature arises close to the star. The shape of the silicate feature from β Pic is nearly identical to that derived from the *ISO* spectrum of 51 Oph; both exozodiacal features are very different from that of the zodiacal light. The exozodiacal features are roughly triangular, peaking at 10.3 μm, while the zodiacal feature is more boxy.
Keywords: zodiacal light, infrared observations, interplanetary dust

1. Introduction

The spectrum of the zodiacal light is a key for understanding the origin of Solar System dust disk and its connection to dust disks around other planetary or planet-forming stellar systems. Theoretically, we expect a distinction between spectra of disks around older and younger disks, as the originally small interstellar dust particles combine to form planetesimals, comets, and asteroids (Beckwith, Henning, and Nakagawa 2000). Young stars have disks dominated by small particles, which produce a silicate feature diagnostic of particle chemistry. Toward the well-studied star β Pic, the 10 μm silicate feature was detected (Telesco et al. 1991) and its substructure measured (Knacke *et al.* 1993). Over the entire infrared spectrum of the well-observed debris disk around the star HD 14257, several silicate features were detected, and these features are by far the dominant structures in the spectra (Malfait *et al.* 1999). For a sample of AeBe stars, silicates are generally present but with significant variations form star to star (Meeus *et al.* 2001). The asteroids and comets of a mature planetary system produce dust via ice sublimation and mutual collisions. While small particles are ejected from the solar system by radiation pressure, larger particles must be continually replenished to balance losses due to Poynting-Robertson drag and fragmentation due to mutual collisions (Grün *et al.* 1985). The differences in particles from star to star may be reflected in the variety of glass with embedded metal and sulfide (GEMS) inclusions in meteorites, some of which look like astronomical silicates characteristic of the diffuse interstellar medium, while others are more crystalline, as seen in the spectra of disks and new comets (Bradley *et al.* 1999). Crystalline silicates like SiC are present in meteorites, and they are thought to originate in the solar system since crystalline silicates are not observed in the ISM, possibly destroyed by supernovae shocks during transport from the envelopes of evolved stars (Demyk *et al.* 2001). Molster, Bradley, and Sitko (2002) suggest that large crystalline silicate grains containing iron (Fe) may have been amorphous grains annealed close to the sun, then transported outwards by turbulence in the early solar disk,

while some Fe-poor crystalline silicates in small grains may have condensed from the gas phase in the inner disk, then transported by radiation pressure *over* the solar disk to distances beyond Jupiter. Interplanetary dust particles captured in the Earth's atmosphere are predominantly silicate minerals with prominent 10 μm features in their absorption spectra (Sandford and Walker 1985). The spectrum of the Solar System dust is a 'laboratory' measurement, because we actually know some of the properties of interplanetary dust by *in situ* observation. The zodiacal spectrum is potentially a key to discriminating between old and young disks around other stars.

The particles that produce the zodiacal light originate from both asteroids and comets. The mix of cometary and asteroidal dust probably varies, depending on particle size, composition, and orbital distribution. New comets produce crystalline particles with spectra similar to young protoplanetary dust disks (Crovisier *et al.* 1997; Hayward, Hanner, and Sekanina 2000). Analyzing the dynamics of particles produced by the 'mature' short-period comet 2P/Encke revealed that it produces only mm-sized and larger particles (Reach *et al.* 2000). The broad-band infrared spectrum of the zodiacal light over 12–100 μm is matched by a model with particles composed of silicates and the same size distribution measured *in situ* by Earth-orbiting satellites (Grün *et al.* 1985; Reach 1988). In addition to size and composition, orbits may distinguish asteroidal and cometary particles. As asteroids are relatively more confined to the ecliptic than comets, we might expect a difference between the mineralogy of the dust between observations in the ecliptic plane and toward the ecliptic pole.

The goals of this paper are to determine whether there is a silicate feature in the zodiacal light and to determine whether there are spatial variations in the spectrum of the zodiacal light. Previous work indicated there may be some structure in the mid-infrared zodiacal light spectrum, but at a level of no more than 15% of the continuum. This result was obtained using the spectrum of the zodiacal light from 5–16 μm measured toward one line of sight as part of the performance verification phase of the *Infrared Space Observatory* (Reach *et al.* 1996). The results showed a hint of a spectral feature with shape similar to that seen from comets (Hanner, Lynch, and Russell 1994; Crovisier *et al.* 1997; Grün *et al.* 2001) and the β Pic debris disk (Knacke *et al.* 1993; Fajardo-Acosta and Knacke 1995). Some evidence for a silicate feature in the zodiacal light was also found from observations with the Infrared Telescope in Space (IRTS) (Ootsubo *et al.* 1998; Ootsubo 2002). It is important not only to determine whether there is a silicate spectral feature but also to constrain its shape. Cometary and β Pic dust have already been shown to have a 10 μm silicate feature with shape different from that of interstellar dust (Draine and Lee 1984) from which Solar System solids formed. Previous observational results for the zodiacal light were inconclusive because of potential detector and optical defects that had not yet been characterized, or because the spectral coverage did not extend beyond the red edge of the silicate feature (IRTS). In this paper, we present follow-up *ISO* observations and analysis of deep archival data that have the optimal sensitivity to the diffuse emission. The new observations include the ecliptic pole, ecliptic plane, and mid-latitudes, and we compare the spectra to determine whether there is evidence for different types of particles overhead as compared to particles in the ecliptic, both near the Earth's orbit and exterior to it.

Then we compare the zodiacal light observations to exozodiacal spectra, to search for similarities and differences between Solar System dust and dust around other main sequence stars.

2. Observations

2.1. Zodiacal light: Observing strategy

The new observations were made using the ISOCAM (Cesarsky *et al.* 1996) instrument on the *Infrared Space Observatory* (Kessler *et al.* 1996). They consist of 3 observing sequences with the circular-variable filter (CVF); two observations were in the ecliptic plane and one was toward the ecliptic pole. The observations in the ecliptic plane were performed as two-epoch, fixed-time observations of the same piece of sky, to measure the change of the brightness with the changing position of the Sun. These observations were scheduled at different times of year such that the solar elongations (ϵ_i) on the two dates are as close as possible to supplemental angles ($\epsilon_1 + \epsilon_2 = 180^\circ$). The widest separation of solar elongations makes it more possible to separate the contributions from the inner and outer Solar System. Taking the visibility constraints of *ISO*, allowing some margin to make it possible to schedule the observations, and choosing the ecliptic plane observations to be taken as far from the galactic plane as possible, the observed lines of sight were toward ecliptic longitude 50.1° and latitude 0.3° with solar elongations $\epsilon_1 = 68^\circ$ and $\epsilon_2 = 113^\circ$. The same astronomical observing template (AOT) configuration was used for each spectrum: 10 frames of 5 sec duration were taken at each step of the long-wavelength circular variable filter (CVF). We used the $12''$ pixel-field-of-view lens in order to maximize the illumination on the detector. Transient gain response is an important limitation of background observations like these, and the timescale for transient response is inversely proportional to the flux on the detector. By using the $12''$ pixel-field-of-view lens and 5 sec integration time, the flux is increased by a factor of 10 relative to the previous ISOCAM zodiacal light spectrum, which allowed us to reach the fainter brightness levels at the ecliptic pole. After each CVF observation, an observation of the same field with three filters (LW6, LW7, and LW8) was concatenated. These observations were used to confirm that the detectors were stabilized during the CVF observations. The observing conditions are summarized in 1.

The ISO Short Wavelength Spectrometer (de Graauw *et al.* 1996) was also used in calibration and discretionary time to obtain deep AOT6 observations ($\lambda/\Delta\lambda \sim 3000$, multiple scans at the longest integration times) for the purpose of detecting the thermal continuum and possible spectral features from zodiacal dust grains. The observations were obtained in revolutions 461, 769, and 836 at positions which corresponded to solar elongations of maximum viewable zodiacal brightnesses. Emission was detected in the 7 to 12 μm range, to within the 1-σ detection threshold for the SWS Band 2 detectors of $\sim$50 MJy sr^{-1}, but the sensitivity was insufficient to allow a search for spectral features. No corrections to the SWS relative spectral response functions for background emission were ever applied, or needed as an outcome of these measurements. The observed brightness was

Table 1: *ISOCAM Observing Log*

			Ecliptic (J2000)		DIRBE		
Project	Day	ϵ	λ	β	4.9 μm	12 μm	25 μm
WREACH.ZODYSP	200	68.9	50.12	0.30	2.03	64.48	79.42
WREACH.ZODYSP	249	113.9	50.12	0.30	0.50	25.82	37.28
WREACH.ZODYSP	118	89.6	0.48	89.48	0.40	13.06	15.50
LUTZ00	334	78.0	324.70	-20.22	1.09	35.08	41.89
LUTZ01	341	81.4	257.81	81.41	0.48	13.83	15.59
LUTZ02	344	74.0	312.29	-61.49	0.63	16.91	18.76
LUTZ03	344	91.5	354.13	-76.94	0.43	13.40	15.53
LUTZ04	345	107.9	49.32	-69.40	0.35	12.55	15.14
LUTZ05	347	88.9	349.60	-18.80	0.84	30.85	38.51
LUTZ06	348	84.5	345.57	-25.85	0.82	27.38	32.97
LUTZ07	352	106.8	17.88	-39.87	0.45	16.91	21.02
LUTZ08	3	104.6	30.58	-36.30	0.47	17.60	21.91
LUTZ09	4	74.8	355.26	-32.59	0.88	25.28	28.96
LUTZ10	9	68.5	353.66	-29.10	1.12	29.65	33.30
LUTZ11	9	72.6	0.75	-10.07	1.56	49.38	59.69
LUTZ12	19	115.6	55.89	-19.27	0.47	20.89	27.77
LUTZ13	25	88.0	32.09	-42.15	0.54	17.54	20.71
LUTZ14	36	75.9	31.53	-10.19	1.31	43.87	53.80
LUTZ15	40	99.4	59.32	3.42	0.78	33.92	45.38
LUTZ16	92	99.6	270.87	30.54	0.52	20.25	25.46

consistent with that predicted by the COBE/DIRBE zodiacal light model (Kelsall *et al.* 1998) described in more detail in §2.3.1.

2.2. Zodiacal light: Archival data

To supplement the dedicated observations described above, we searched for archival *ISO* data suitable for deriving zodiacal light spectra. We concentrated only on ISOCAM CVF data, which is by far the most sensitive data for this task. We attempted to derive a zodiacal light spectrum from the deepest spectrometer (SWS) data, but the spectra were inadequate because the zodiacal light was too faint in comparison to the dark current.One ISOCAM program in particular, DLUTZ.ZZULIRG, was ideal for use because (1) their intended targets were faint (< 70 mJy); (2) the targets were expected to be point-like; (3) the observations are very deep (over 2 hours per pointing); and (4) the spectra were taken *aller-retour*, i.e. rotating the CVF toward increasing

wavelengths and then back toward decreasing wavelengths. The scientific results on the intended targets were presented by Tran *et al.* (2001). Table 1 shows the observing parameters for these observations; we will refer to specific archival spectra by the sequential numbers listed after 'LUTZ' in this table.

2.3. Zodiacal light: Data reduction

2.3.1. Dark current and zero-point

The observations were analyzed using routines developed at the *Institut d'Astrophysique Spatiale* (IAS) as part of the pre-launch calibration of ISOCAM and the performance verification (PV) phase of the *ISO* mission. For each image, we used a dark-current image obtained during the PV phase. To correct for the drift of the dark current between PV phase and the epoch of observation, a correction was obtained using the portion of ISOCAM that is not illuminated with the 12" lens and Fabry mirror combination. We avoided the region near the outer edge of the Fabry mirror, which was contaminated by stray light. The uncontaminated 'skirt' region was correlated pixel-for-pixel with the library dark. The library dark was offset and scaled using the zero-point and slope of this fit, and then it was subtracted from each image.

The brightness at the shortest wavelengths was then then compared to the predicted brightness of the zodiacal light. Our model is essentially identical to the one derived by the *Cosmic Background Explorer* Diffuse Infrared Background Experiment (COBE/DIRBE) (Kelsall *et al.* 1998). This three-dimensional structure of the interplanetary dust complex includes a smooth, tilted dust cloud, which dominates the brightness, as well as anisotropies due to the Earth's resonant dust ring (Dermott *et al.* 1994; Reach *et al.* 1995) and the asteroidal dust bands (Dermott *et al.* 1984; Reach *et al.* 1997). The wavelength-dependence is through the Planck-function kernel of the brightness integral as well as a set of albedoes and emissivities for each of the 10 DIRBE wavelebands spanning 1.25–240 μm. We have generalized the model so that it predicts the brightness at an arbitrary wavelength (Reach 2000). We replaced these values with smooth curves for the wavelength-dependent emissivity and albedo. Similarly, the scattering phase-function, which was parameterized separately for each DIRBE waveband, was replaced by an interpolation between the phase functions DIRBE-derived phase functions. At ISOCAM wavelengths, scattering is only a very minor contributor to the brightness. Zodiacal model predictions were made for the appropriate celestial coordinates, observing date, and wavelength of each CVF observation. A small offset was then applied to the ISOCAM data, to make the brightness at 5.5–6 μm match the COBE/DIRBE model.

2.3.2. Transient response of the detectors

These observations are at low light levels, where the observed brightness can be affected by transient gain response and memory effects in the detectors. We carefully checked that the detectors were measuring the actual spectrum of the sky as the CVF was rotated (as opposed to long time-constant transient gain responses). To this end, the IAS transient correction method (Coulais *et al.* 2000) was applied. This method is a straightforward calculation that does not involve fitting to the data and is specified by few parameters. The transient correction was verified by comparing the spectra taken with the CVF rotating in both the increasing- and decreasing-wavelength directions. The transient effect makes the detector output rise more slowly than the signal input; thus, when the brightness was increasing, the observed signal is lower than the true signal. Figure 1 shows the results of the transient correction. The first half of the observation was taken in the decreasing-wavelength, decreasing-brightness direction, where the transient corrections were smaller. After correction, the decreasing- and increasing-wavelength spectra are consistent to within 1–2% of their average, with the decreasing-wavelength spectrum consistently brighter. This suggests that part of the transient gain response has not been corrected, but there is relatively little structure as a function of wavelength that could affect detection of spectral features. We incorporate the differences between the spectra taken in each direction into the systematic errors.

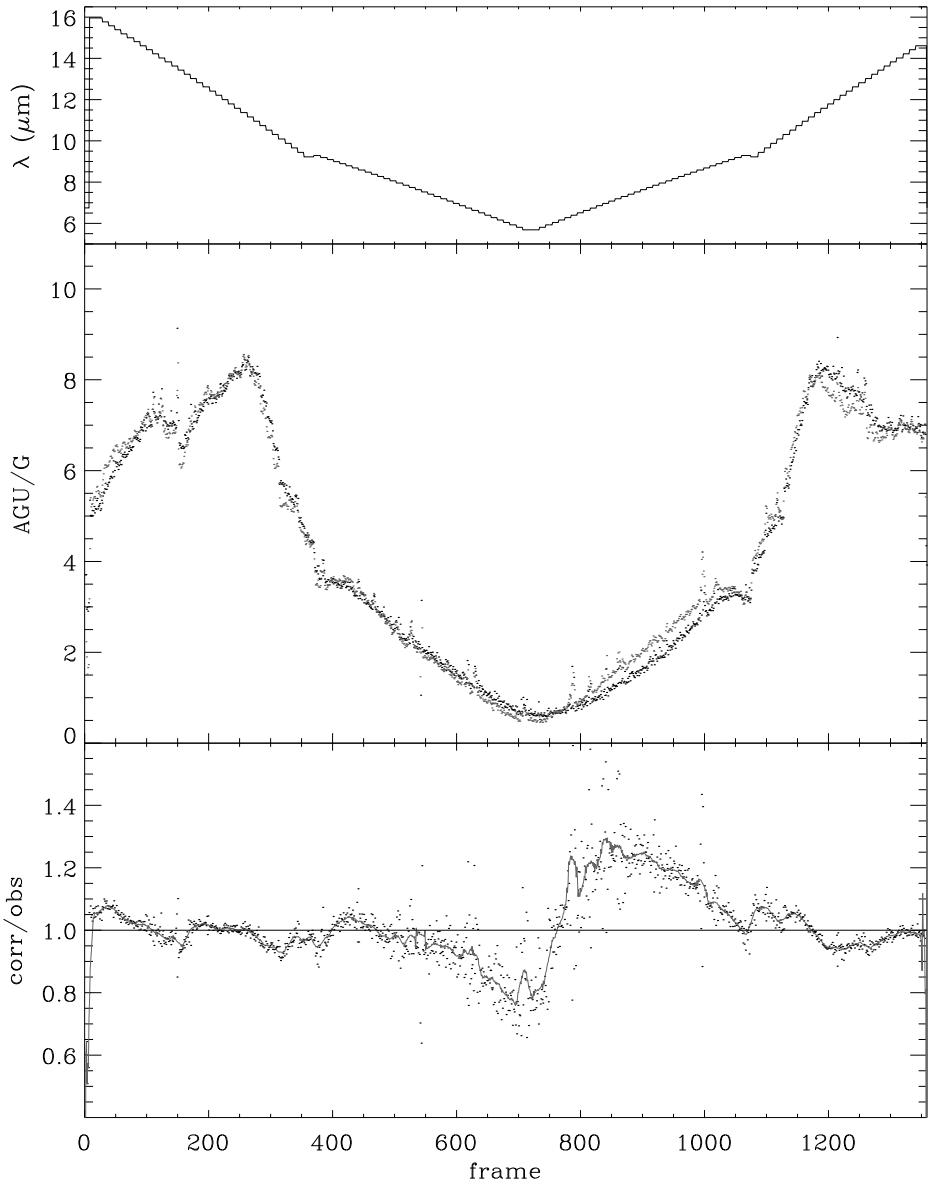

Fig. 1.— Illustration of the correction for ISOCAM CVF transient gain response. *(a)* The top panel shows the wavelength as a function of frame number for the observation of the north ecliptic pole. The CVF was cycled from long to short wavelength, then back up. *(b)* The middle panel shows the brightness (in electrons per second) averaged over the central part of the each frame. One set of dots shows the original data, and another set of dots shows the transient-corrected data. The detector response for decreasing signals is faster than that for increasing signals, so the observed and corrected data are very similar for the first half of the observation. The time constant for transient response is longest for low brightness levels, so the largest deviations are near the

beginning of the second half of the observation, where the sigla was weak and increasing. *(c)* The bottom panel shows the transient correction factor (corrected divided by observed brightness) as a function of frame number.

2.3.3. Stray light removal

A new and significant correction to the spectra was to remove stray light (Okumura 2001). This effect was a significant limitation of our previous attempt to measure the absolute sky spectrum (Reach *et al.* 1996). Absolute measurements are most prone to stray light because it is exceptionally difficult to differentiate diffuse stray light from the true sky background. Most flat-field calibration observations include stray light, which is desired because the stray light represents a real background to the detector. For the present problem of separating stray light from the true background, we used dedicated calibration observations of a point source observed over the range of CVF wavelengths and at two different locations on the array. Comparing the background observed through all of the ISOCAM filters, spanning 4.5–15 μm, to the brightness observed with the CVF reveals systematic differences that we attribute to stray light in the CVF.

A point source observed through the CVF generates 'ghost images' on the array; the ghosts move as the source is moved. The ghost images are due to multiple reflections in the optics, and these reflections will affect the diffuse emission in a manner similar to the point sources. The diffuse stray light amplitude should be equal to the average amplitude of the ghost images for point sources located all over the array. In practice, we only have calibration data for two pointings of the point source on the array. Thus, we are forced to assume that the wavelength-dependence of the stray light for uniform illumination is the same as that of the average of the ghost amplitudes for two pointings on the array.

For both pointings of the calibration point source, the ghost fluxes were measured and normalized to the main point source flux. This clearly showed the spectral dependence of the ghost intensity. We used the average of the ghost flux spectra for the two pointings of the calibration star to extrapolate the ghost intensity of the point source to the zodiacal light photometric region of the detector; see Blommaert *et al.* (2001) for further detail. ISOCAM was calibrated using the central point-spread-function of stars (not including the ghost images) so that extended emission (which includes stray light) must be corrected. The stray light amplitude depends on wavelength: it decreases monotonically from 35% at 6 μm to 20% at 9.3 μm near the edge of the short-wavelength CVF; then for the long-wavelength CVF it jumps to 30% at 9.5 μm, decreasing to 6% at 15.3 μm. The stray-light correction is discontinuous across the boundaries between the two CVFs at 9.5 μm. This agrees with each of our zodiacal light observations, which showed a significant discontinuity before stray-light correction. The stray-light correction was validated by comparing to data taken through 9 different ISOCAM filters. The filter data have very coarse spectral resolution ($\lambda/\Delta\lambda \sim 5$), but they do not suffer as much from stray light because the filters are tilted with respect to the detector. To compare the filter and CVF data, we first divided each

intensity measurement by the DIRBE zodiacal light model (§2.3.1) appropriate for the observing date, direction, and wavelength. Figure 2 shows the comparison between the CVF and filter data (Blommaert *et al.* 2001). The spectra will be discussed in detail in the remainder of this paper, but this figure is shown in advance as a calibration validation. Before correction, there were clear discrepancies between the CVF and filters. After correction, the two types of observation agree well. Both the filters and CVF seem to show systematic deviations, at the 10% level, from the DIRBE zodiacal light model.

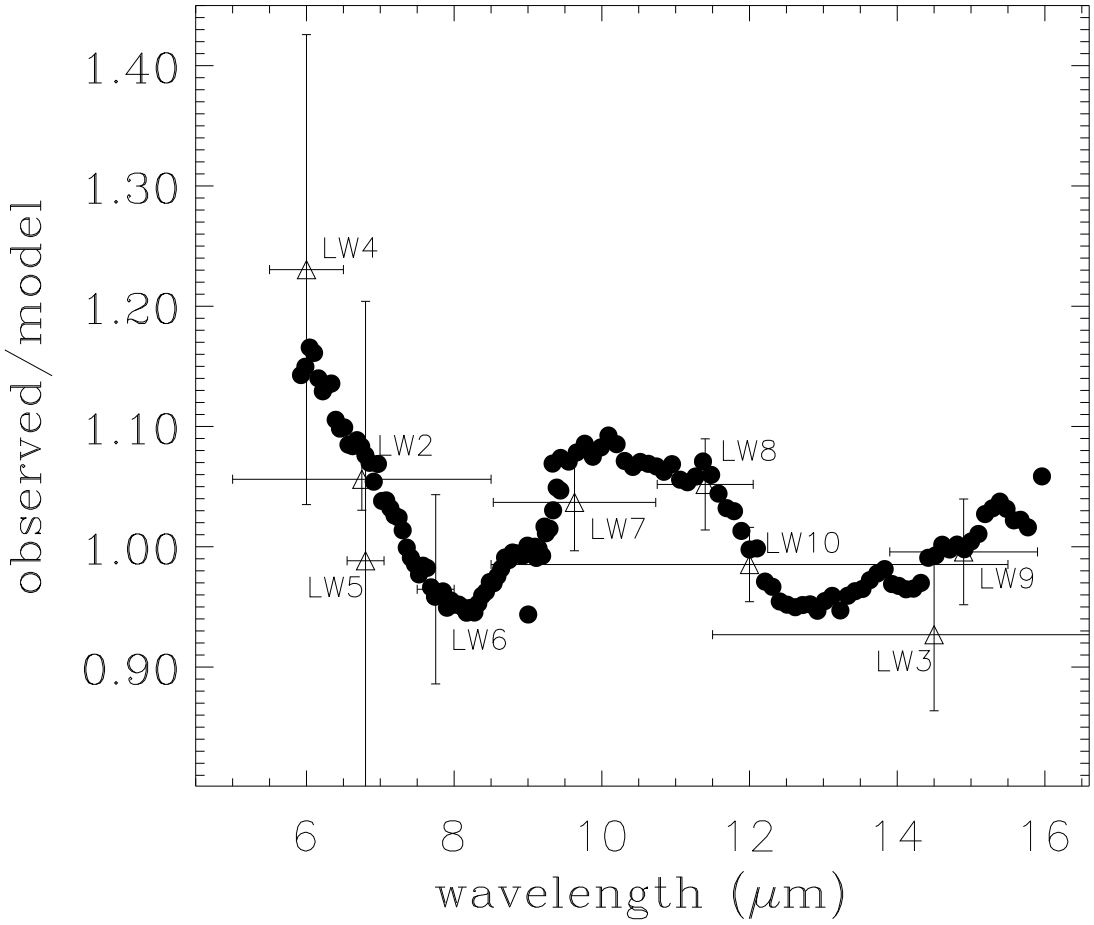

Fig. 2.— Comparison between the sky brightness observed through the broad, tilted filters (triangles with error bars) and through the circular-variable filter (filled circles). Each data point presents the observed sky brightness after all corrections described in the text, divided by the COBE/DIRBE zodiacal light model appropriate for its wavelength and observing date and direction.

2.3.4. Spectra

The stray-light-corrected, transient-corrected, dark-subtracted data cubes were averaged at each wavelength step of the CVF. The pixel-to-pixel vignetting variation was normalized by dividing each image by a carefully-reduced zodiacal light observation obtained during a dedicated calibration orbit during the mission (Biviano *et al.* 1998). The final spectra were generated by averaging over the central 12×12 pixels ($2.4' \times 2.4'$). Figure 3 shows the results. The spectra are generally similar to each other, modulo a scale factor. They all show a similar structure in the 9–11 μm range.

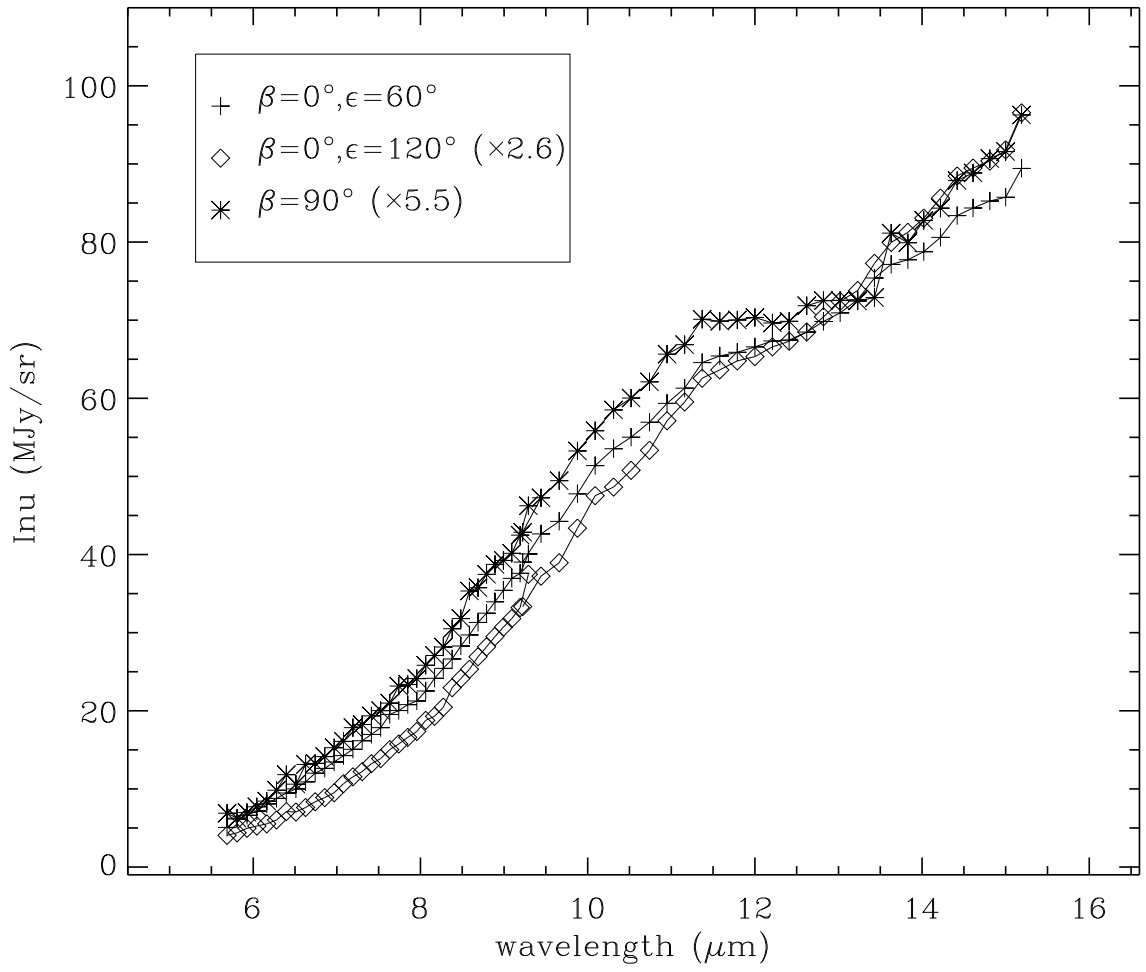

Fig. 3.— Spectra of the zodiacal light taken on three lines of sight representing the extremes of the *ISO* operational pointing zone: in the ecliptic plane at 60° and 120° solar elongation, and toward the north ecliptic pole. The spectrum in the ecliptic toward $\epsilon = 120°$ was scaled by a factor of 2.6, and the spectrum of the ecliptic pole was scaled by a factor of 5.5 in order to fit on the same scale

as the $\epsilon = 60°$ spectrum.

2.3.5. Reduction of archival data

The reduction of the archival spectra used the final, revolution- and position-in-orbit-dependent dark current calibration for the $6''$ lens Blommaert *et al.* (2001), as well as the final spectral calibration and stray light correction described above. The fields were mostly clean of interstellar cirrus, and they spanned a useful range of ecliptic coordinates and solar elongation. Three of the lines of sight (numbers 16, 15, and 12 in Table 1) pass through significant amounts of interstellar medium. One of them (number 16) is at a relatively low galactic latitude of 13°, so interstellar contamination is not surprising. The other lines of sight are at high galactic latitude; however, two of the lines of sight (numbers 15 and 12 in Table 1) pass through high-latitude molecular clouds evident in far-infrared excess (Reach, Wall, and Odegard 1998). In the analysis below, we will separate the three lines of sight contaminated by the interstellar medium (ISM) form the clean, zodiacal spectra. The spectra are shown in 4.

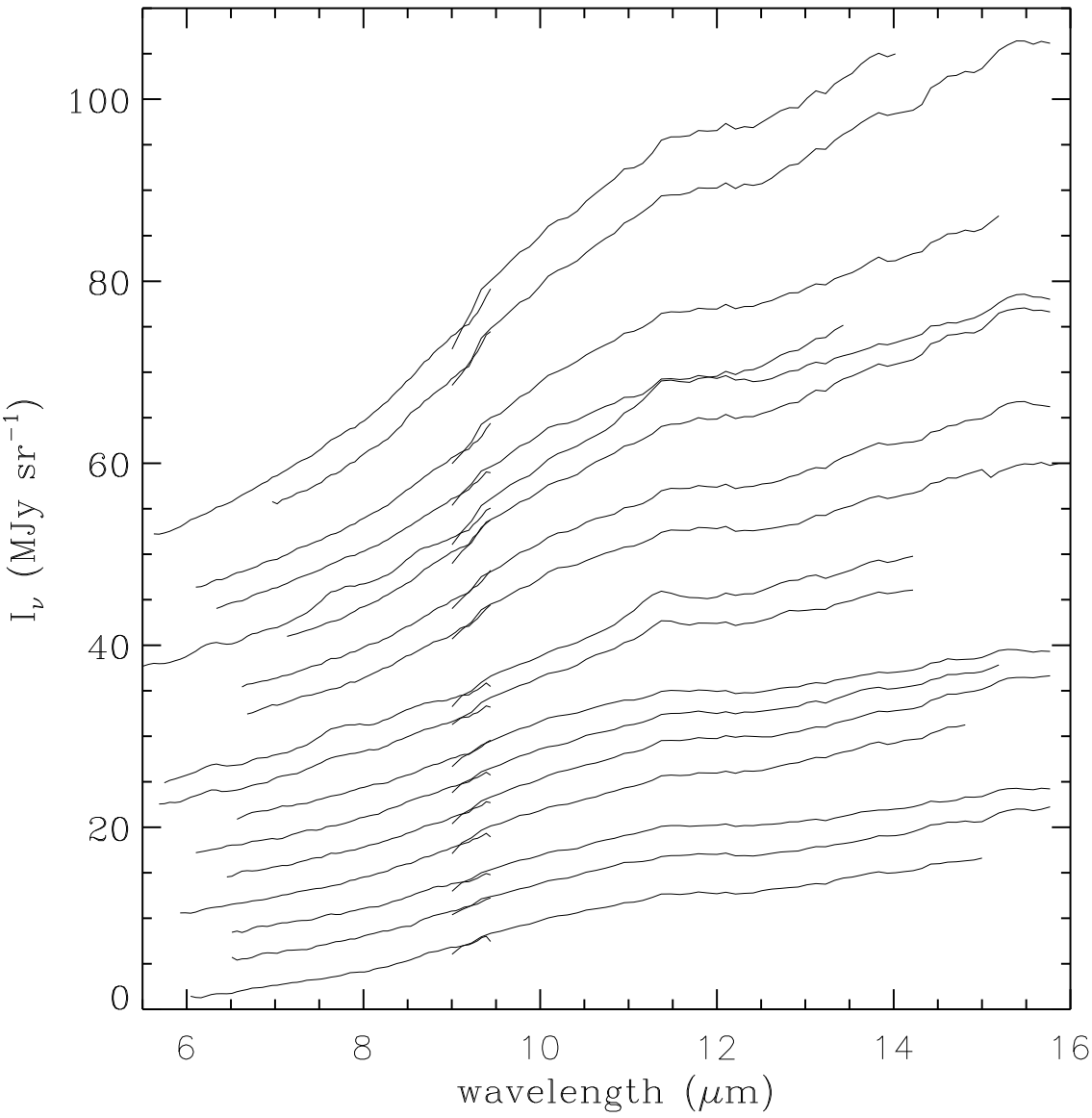

Fig. 4.— Spectra obtained from the deep archival observations with the 6″ pixel field of view lens. Each spectrum is toward a different solar elongation and latitude. They were sorted in order of brightness and offset vertically from each other by 3 MJy sr^{-1} for clarity.

2.4. Exozodiacal light

2.4.1. CAM Observations

We reanalyzed the archival observations of β Pic that were first presented by Lagage *et al.* (1999). The data were taken in a manner similar to the zodiacal light observations described above, except the highest magnification (1.5″ pixel field of view) lens was used. The analysis of the data cube (images at each wavelength) was also similar. To derive the spectrum of β Pic, we measured the flux within a circular aperture (10.5″ diameter) after subtracting an annular average background (to 22.5″ diameter) at each wavelength.

2.4.2. SWS Observations

Observations of β Pic have been obtained with the ISO SWS (de Graauw *et al.* 1996) in AOT6 mode in programs of CWAELKEN (CRYSTAL and CRYSTAL2) and DBOCKELE (VEGA_ICE), variously covering the full 2.4−45.2 μm range available between the two grating sections. Pantin (Waelkens) and Malfait *et al.* (1999) have presented the observations from the CWAELKEN programs. We have reprocessed the three sets of observations with the latest pipeline software (compatible with the ISO pipeline OLP10.1) and interactive techniques to detect and correct the effects of cosmic radiation on the scan data and dark currents. These effects are manifest as spurious jumps in signal levels, and drastic degradation in S/N ratios over SWS bands 2 (7–12 μm), 3 (12–39.5 μm), and 4 (39.5–45.2 μm) where the β Pic flux levels are already in the dark-current dominated signal regime. We have interactively treated these effects on a detector and scan basis, significantly improving the S/N ratios and removing artifacts. (Some such artifacts were visible in the earlier reductions, including band 4, where Pantin (Waelkens) and Malfait *et al.* (1999) substituted SWS Fabry-Perot data provided serendipitously but with unverifiable calibrations.) Then we coadded the corrected products and reduced these to final 1-D spectra rebinned to the resolution of the instrument. This paper is focused on the ISOCAM CVF wavelength range. We present the 5–16 μm range of the SWS spectrum in Figure 5. We mention in passing the presence of CO and H_2O gas absorption lines near 4.0 and 6.2 μm, respectively, with strengths and amplitudes comparable to those identified in 51 Oph by van den Ancker *et al.* (2001).

2.4.3. Spectrum β Pic

Figure 5 shows the spectrum of β Pic from 5 to 16 μm. The broad-band photometric points obtained with ISOPHOT (Heinrichsen *et al.* 2000) and *IRAS* are overlaid; they show that the absolute calibration of the SWS and PHOT spectra agrees. The IRTF observations of Knacke *et al.* (1993) and the ISOCAM observations are clearly different from the SWS observations, with

the former being significantly fainter at wavelengths beyond 10 μm. The Knacke *et al.* (1993) observations cover enough of the short-wavelength, pure photosphere part of the spectrum (beyond the left-hand-edge of Fig. 5) that we can see that the SWS and IRTF data agree well for the photosphere. The CAM data also agree in calibration with SWS at the shortest wavelength 5.92 μm. The differences between the spectra, which begin around 8 μm and become very large at longer wavelengths, are due to the circumstellar material. The dust disk begins to dominate over the stellar photosphere beyond 8 μm wavelength; by 10 μm, the circumstellar material is as bright as the photosphere. The aperture of the SWS and PHOT observations is significantly larger than that of the CAM and IRTF observations, and the colder part of the debris disk is clearly extended. The disk is clearly resolved in ground-based 10 μm observations (Pantin, Lagage, and Artymowicz 1997), but its extent is only a few arcsec. The warm, inner disk is completely contained within all of the apertures discussed here. But at longer wavelengths, the disk is clearly extended, with a full width at half-maximum of $8.7 \times 2.9''$ at 25 μm (Heinrichsen *et al.* 2000). The disk was also resolved in the longer-wavelength CAM CVF images (Lagage *et al.* 1999). Thus the CAM and IRTF observations detect primarily the inner disk, while the SWS and PHOT observations contain essentially the entire disk including the colder emission.

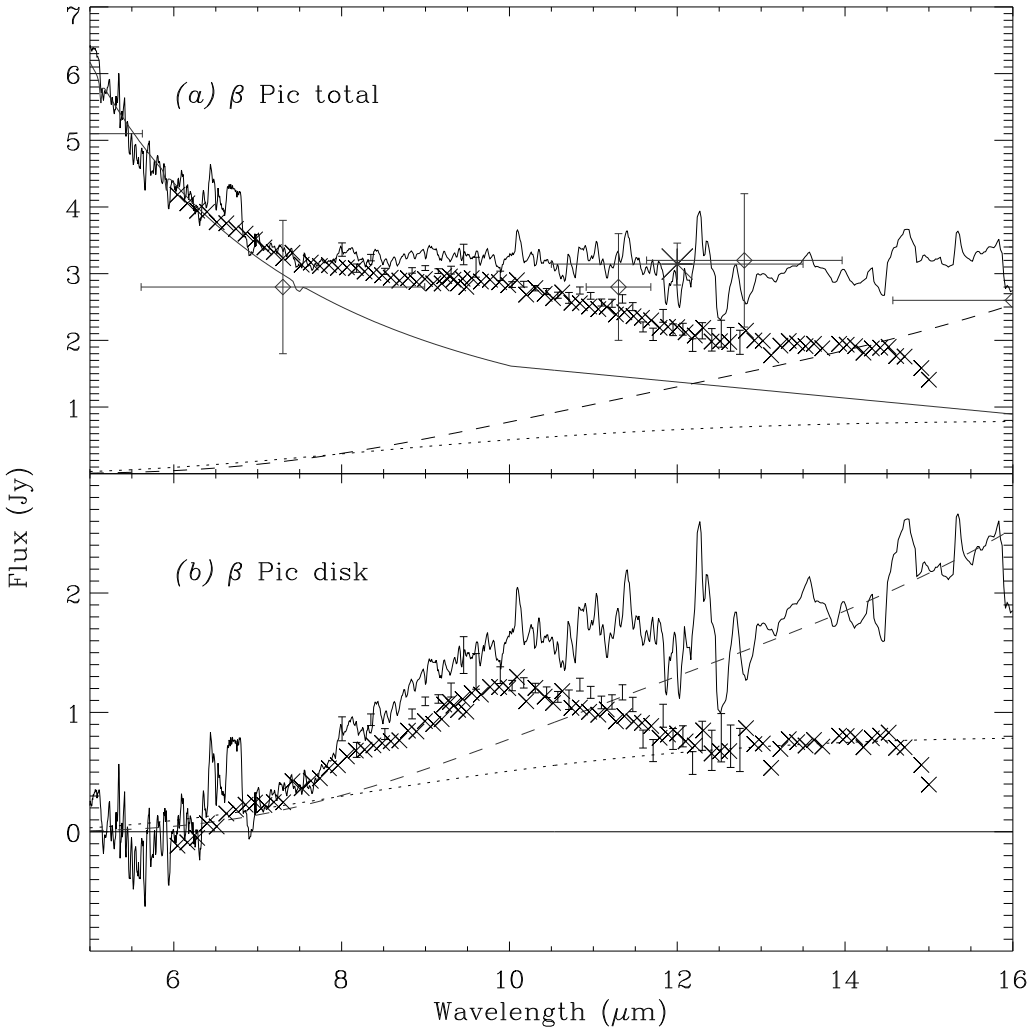

Fig. 5.— *(a)* Spectrum of β Pic obtained with the ISO SWS (jagged curve), CAM (X symbols) and IRTF (I symbols). The broadband photometry from ISO PHOT (diamonds with large error bars) and IRAS (asterisks with error bars) are overplotted in grey. The Kurucz model stellar photosphere, normalized to the 2.4–4 μm ISO SWS flux, is shown as a solid line. Approximate models for the debris disk spectra are shown for the SWS spectrum (dashed line) and the CAM and IRTF spectra (dotted line). The differences between the observed spectra are primarily due to different observing apertures, as the SWS and PHOT data were taken with a large aperture that includes the entire cold debris disk. *(b)* Circumstellar spectra of the β Pic disk obtained by subtracting the stellar photosphere from the observed spectra. The curves and symbols are the same as in panel *(a)*. The double-peaks at 6.4–6.8 μm in the SWS spectrum are due to H_2O.

The lower panel in Figure 5 shows the disk spectrum, obtained by subtracting the Kurucz 1993 ATLAS model, kp00_8250(g45) scaled to match the flux at 2.5–3 μm, for the stellar photosphere.

The disk spectrum is complicated, being due to a combination of particles both far from the star, which produces the extremely bright far-infrared emission peaking around 60 μm (Heinrichsen *et al.* 2000), and warmer dust that produces the mid-infrared emission (Pantin, Lagage, and Artymowicz 1997). We will discuss these spectra and their decompositions below in § 6.

3. Results: Continuum plus silicate feature in the zodiacal light

The mid-infrared zodiacal spectra are dominated by a smoothly increasing brightness as a function of wavelength, due to thermal emission from dust at ~ 270 K, with a broad shoulder at 9–11 μm. To remove the continuum from the spectra, we used a model for the zodiacal light that predicts the surface brightness as a function of wavelength for each target position and observing date (§2.3.1). We also fitted each spectrum to a single blackbody in order to characterize the continuum independent of the model. Table 2 shows the temperature and optical depths of the continuum spectral fits.

Table 2: Blackbody fits and color ratios

Spectrum	T (K)	$10^7\tau$	Δ_{sil}
ZODY_60	268.5 ± 0.4	2.45 ± 0.02	5.5 ± 0.1
ZODY_120	244.1 ± 0.6	1.48 ± 0.02	5.2 ± 0.7
ZODY_NEP	274.0 ± 1.1	0.44 ± 0.08	7.0 ± 2.0
LUTZ[b]	269.6 ± 5.6	0.92 ± 0.40	6.9 ± 1.0
LUTZ[c]	267.1 ± 0.4	0.93 ± 0.01	8.2 ± 0.7

[b] average ± rms from the deep Lutz spectra (excluding those contaminated by interstellar medium)
[c] weighted average and statistical uncertainty from deep Lutz spectra (excluding those contaminated by interstellar medium)

Fig. 6.— Comparison of the ISOCAM spectra (symbols, as in Fig. 3) with the DIRBE zodiacal light model for the same coordinates and date (large errors bars and solid line).

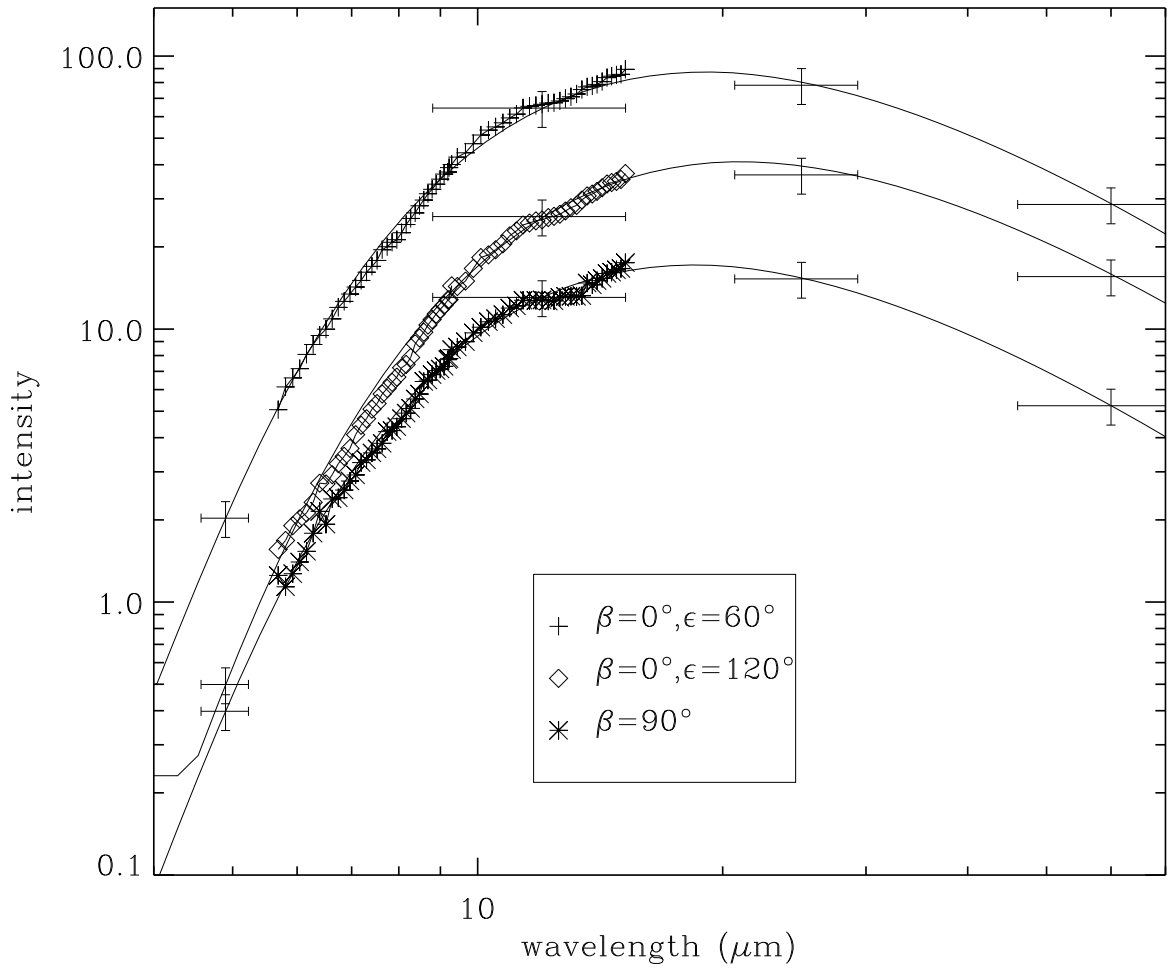

Fig. 7.— Ratio of the observed zodiacal light spectra from Fig. 3 to a blackbody continuum. The continuum was fit using only wavelengths outside of 9–11 μm.

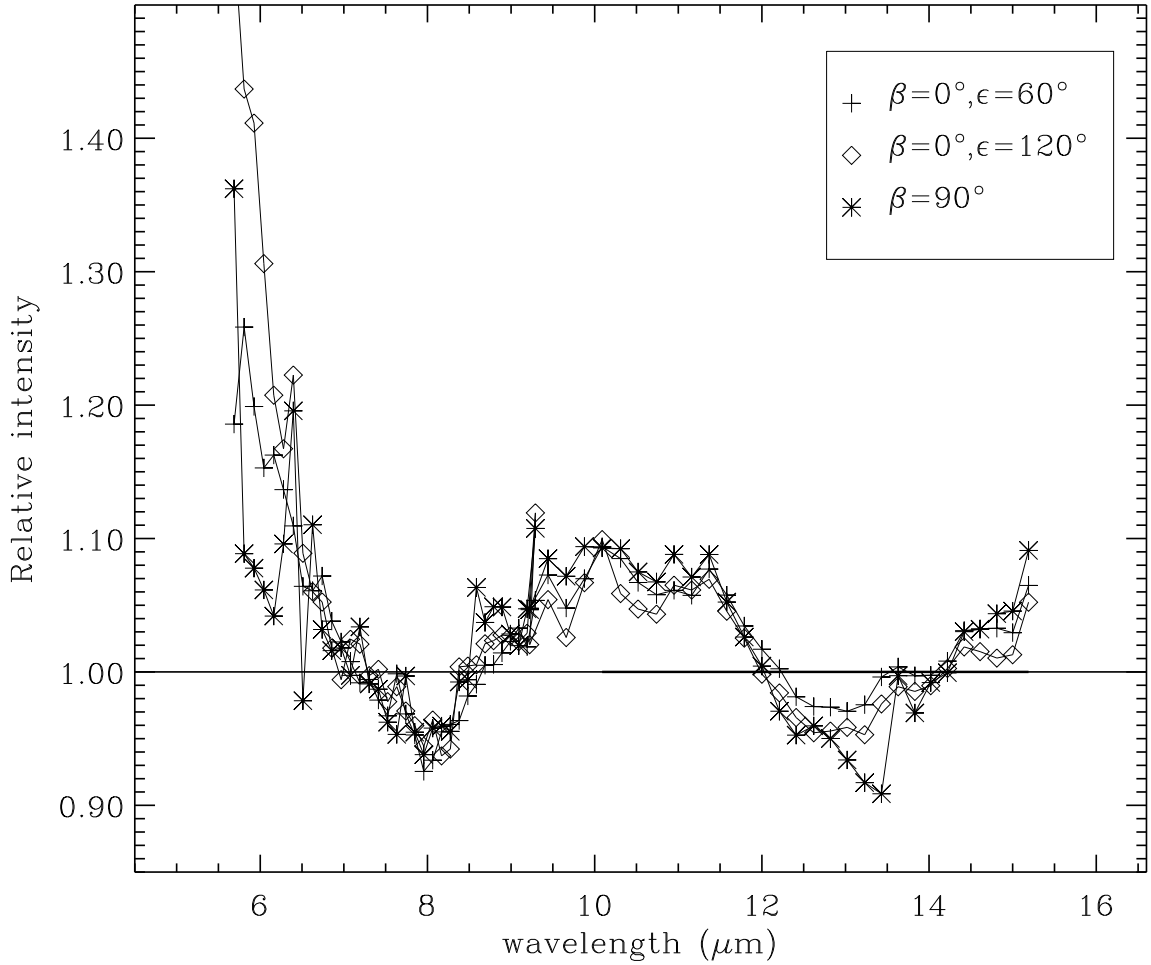

Figure 6 compares the observed spectra to the their corresponding DIRBE zodiacal light model predictions. Figure 7 shows the observed spectra divided by their corresponding DIRBE zodiacal light model predictions. Because the model includes only a blackbody emissivity, the ratio spectrum should reveal all structures in the spectrum—both narrow lines and broad bands. It is clear that the model very accurate predicts the spectra: it matches to within 10%, with no adjusting of the model to fit the new ISOCAM data. Because of the excellent agreement between the COBE/DIRBE model and the ISOCAM data, and because the COBE/DIRBE data span a much wider parameter space of spatial and wavelength coverage, we need not delve into a detailed model for the zodiacal brightness distribution in this paper, but instead we refer the reader to Kelsall *et al.* (1998). The value of the new results presented here is in measuring the spectrum of the zodiacal light at a spectral resolution sufficient to detect spectral features.

The ratio of the observed (ISOCAM) to model spectra shows clear systematic structures. This structure consists of a well-defined, broad peak at 9–11 μm, superposed on an overall

'bowl'-shaped residual. The 9–11 μm feature is the same structure as was seen in our earlier mid-infrared zodiacal light spectrum (Reach *et al.* 1996), but now we have sufficient signal-to-noise and confidence in the instrumental calibration to confirm a detection. The 9-11 μm excess has also been detected in data from the Mid-Infra re Spectrometer (MIRS) on the Infrared Telescope in Space (IRTS) by Ootsubo *et al.* (1998), although the MIRS data extend in wavelength only to 11.59 μm, which was not quite long enough to see the return from the feature to the continuum at long wavelengths. The 'bowl' shape is due to the DIRBE model not accurately predicting the shape of the continuum. As discussed below, the zodiacal light emissivity is a superposition of emission from particles of many sizes (each with their own temperatures) as well as particles at many locations (also having their own temperatures). The DIRBE model incorporates the spatial dependence of the temperature, but it assumes a single blackbody at each location, which is not strictly true. Because the overall shape of the continuum is best studied with data covering an even wider range of wavelengths than ISOCAM, we will emphasize the 9–11 μm feature in this paper and briefly discuss the continuum shape in comparing with the wider DIRBE wavelength coverage.

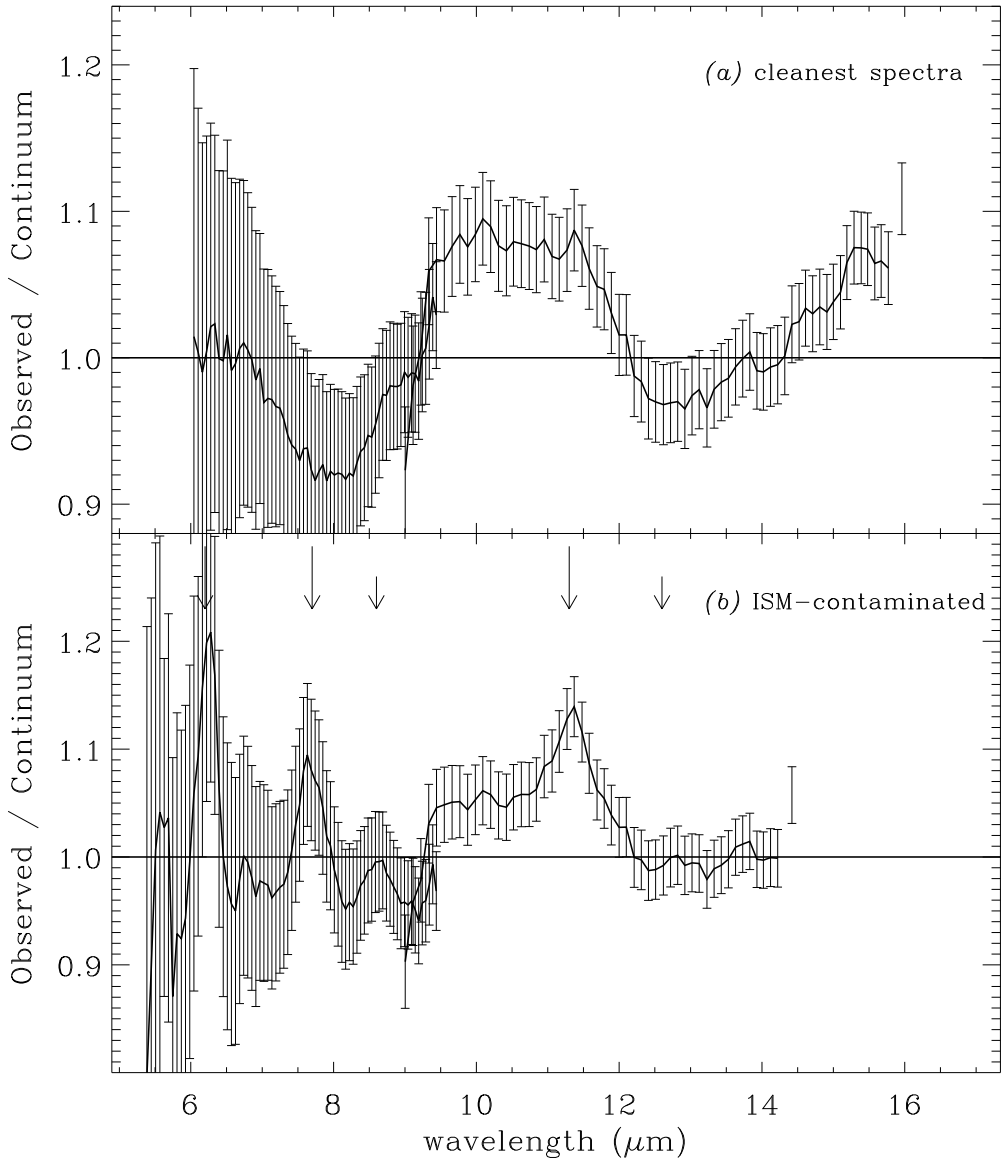

Fig. 8.— Ratio of the archival zodiacal light spectra, taken with the 6″ lens and CVF of ISOCAM, to a zodiacal light model. The top panel shows the average of the observed to continuum ratios for the 14 spectra with no evidence for interstellar contamination. The bottom panel shows the average for the 3 spectra with interstellar contamination. The ISM lines, attributed to polycyclic aromatic hydrocarbons (PAH), are labeled with vertical arrows.

Figure 8 shows the average of the archival spectra divided by their continuum from the DIRBE zodiacal light model. The three ISM-contaminated spectra were treated separately. They clearly show bright infrared bands at 6.2, 7.7, and 11.3 μm. These are the brightest emission bands in spectra of diffuse interstellar matter, and they are widely attributed to polycyclic aromatic

hydrocarbons (PAH) (Boulanger *et al.* 1996). The uncontaminated spectra show no such interstellar lines, but instead they are dominated by the same broad band at 9–11 μm that was seen in the dedicated zodiacal light observations. One straightforward result of the ISOCAM observations is that there are no PAH bands from the zodiacal light. The PAH bands are bright from the interstellar medium because of the presence of very small grains and a pervasive UV-bright radiation field that transiently heats the grains to high temperatures. In the Solar System, the interval between successive photons is shorter, and the particles will be close to their equilibrium temperature. This temperature is still hot enough so that the mid-infrared bands would be excited. The upper limit to PAH bands from the zodiacal light is $< 2\%$ of the continuum brightness.

All of the zodiacal spectra, including the dedicated observations toward the ecliptic plane and pole (Fig. 7), the deep, archival observations (Fig. 8) and observations through the wide-band filters (Fig. 2), show an excess in the 9–11 μm range that is characteristic of silicates. To characterize the brightness of the silicate feature, we define the quantity

$$\Delta_{sil} = 100 \left(\frac{\langle I_\nu \rangle_{(9-11\mu\mathrm{m})}}{\langle \tau B_\nu(T) \rangle_{(9-11\mu\mathrm{m})}} - 1 \right),$$

which is the percentage excess of the observed spectrum I_ν relative to the blackbody fit $\tau B_\nu(T)$ (where τ and T are the fitted optical depth and temperature and B_ν is the Planck function) averaged over the wavelengths of the feature. Table 2 shows the values of Δ_{sil} for the zodiacal spectra. To first order, the continuum and 9–11 μm feature shapes and amplitude are comparable for all of the spectra. The amplitude of the 9–11 μm excess seen in the IRTS/MIRS data (Ootsubo 2002) is similar to that of our data. We present a more detailed comparison of the spectral shapes and systematic dependence on the viewing geometry in section 5.2.

4. Comparison to theoretical models

4.1. Compositions

We calculated the infrared emission spectra for a range of particle compositions and size distributions, to learn what kinds of particles can create the observed zodiacal light spectra. Table 3 describes the particle compositions and optical constant data that we used. The calculations are an update of those that were performed to interpret the 12–100 μm broad-band colors of the zodiacal light (Reach 1988). We are restricting our calculations to plausible materials. The earlier calculations showed that pure, crystalline silicates are too cold (because they are nearly transparent to sunlight) while carbonaceous dust is too hot (because it absorbs sunlight so well). Furthermore, it is unlikely that extremely pure solids will exist in comets. Solids in the Solar System formed from interstellar dust, so we consider interstellar silicate dust as an indicator of the purity of the building blocks. A model for the optical constants of 'astronomical silicates' (Draine and Lee 1984; Laor and Draine 1993) was found to be reasonably

approximated by a volume mixture of pure andesite and 3% graphite (Reach 1988). Extensive infrared observations of C/Hale-Bopp demonstrated that even the silicate dust from a new comet is impure: pure silicate temperatures were too low to produce the observed continuum shape and silicate feature ratios (Grün *et al.* 2001). (We confirm that this is true for many pure silicates; however, some amorphous silicates at 2.82 AU from the Sun have temperatures that are in the range [$T \sim 180$ K] required to explain the Hale-Bopp spectrum without need for extra absorption.) For this paper, we 'dirtied' the pure silicates to the same degree as the 'astronomical silicate' model of Draine and Lee (1984). Specifically, we use the Maxwell-Garnet mixing rule to add amorphous carbon with a volume filling factor f_{car} (listed in Table 3) such that the Fresnel transmittance averaged over the wavelength range 0.2–0.7 μm (where sunlight does most of its heating) is at least $T_{vis} \geq 0.93$, the value for astronomical silicate.

Table 3: Particle compositions and optical data

Name	wavelength range	reference	f^a_{car}
astronomical silicate *(a)*	0.001–1000 μm	Laor and Draine (1993)	...
amorphous olivine (Jena)	0.2–500 μm	Dorschner *et al.* (1995)	0
amorphous forsterite	0.043–61.7 μm	Scott and Duley (1996)	0.1
amorphous pyroxene	0.2–500 μm	Dorschner *et al.* (1995)	0
crystalline olivine *(c)*	0.01–2980 μm	Mukai and Koike (1990)	0.05
crystalline pyroxene *(d)*	6.66-487 μm	Jäger *et al.* (1998)	0.033
crystalline enstatite $\parallel$	0.043–99 μm	Jäger *et al.* (1998)	0.58
crystalline enstatite $\perp$	0.043–99 μm	Jäger *et al.* (1998)	0.58
montmorillonite *(e)*	0.023–2000 μm	Koike and Hiroshi (1990)	0.46
glassy carbon	0.2–100 μm	Edoh (1983)	...
amorphous carbon *(f)*	0.105–800 μm	Preibisch (1993)	...
SiC	0.001–1000 μm	Laor and Draine (1993)	...
Mg-rich crystalline olivine	0.2–8000 μm	Fabian *et al.* (2001)	0.37

4.2. Absorption efficiencies

For each particle composition, the absorption efficiency was computed on the same wavelength grid on which the laboratory optical measurements were provided. The computations were performed for particles radii on a logarithmic grid from 0.11 to 1000 μm (particle mass 10^{-14} to 10^{-2} g). The calculations used Mie theory, and they were somewhat computationally intensive due to the inclusion of very large particles. The grain temperatures we calculated by balancing the solar radiation at 1 AU by the integrated thermal emission of the grains. The grains are assumed to be isothermal, rapidly rotating spheres; thus, absorption was assumed to occur into an effective cross-section πa^2, and emission out of $4\pi a^2$, where a is the particle radius. The

largest grains can conceivably support a small temperature gradient, meaning they would emit at slightly higher temperatures than we have calculated.

4.3. Size distributions

The volume emissivity is calculated by integrating over the size distribution

$$\mathcal{E}_\nu = \int \frac{dn}{da} B_\nu[T(a)] \pi a^2 Q_{abs}(a) da, \tag{1}$$

where dn/da is the size distribution, B_ν is the Planck function, a is the particle radius, and Q_{abs} is the absorption efficiency. In practical units $\mathcal{E}_\nu$ is in MJy sr^{-1} AU^{-1} or in cgs units, erg s^{-1} Hz^{-1} cm^{-3} sr^{-1}. For our calculations, we use the following size distributions. The 'interplanetary' and 'lunar' size distributions are based on a combined analysis of particle detectors on Earth-orbiting satellites, meteors, and lunar microcraters; the only difference between these distributions is for the smallest particles, where the 'lunar' distribution uses the raw lunar microcrater data, while the 'interplanetary' distribution uses an estimate based on β-meteoroid production (Grün *et al.* 1985). The 'interplanetary' size distribution remains the best estimate of the size distribution of cosmic material at 1 AU from the Sun, and it has recently been shown to be consistent with the sizes of particles inferred from the *Long Duration Exposure Facility* (*LDEF*) spaceward face (McDonnell and Gardner 1998). Three other size distributions are included for comparison. The 'interstellar' size distribution is a power-law, $dn/da \propto a^{-3.5}$, as inferred from the interstellar extinction curve (Mathis, Rumpl, and Nordsieck 1977; Draine and Lee 1984); this is not intended to represent the size distribution of actual interstellar grains in the Solar System—the Ulysses and Galileo experiments have clearly shown that small interstellar grains do not penetrate into the inner Solar System (Landgraf *et al.* 2000)—but rather it is included as a simple model for comparison. The 'halley' size distribution is based on analysis of the particle detector data from the P/Halley encounter (Lamy, Grün, and Perrin 1987); it may represent the input size distribution for cometary particles that contribute to the zodiacal dust cloud. Similarly, the 'hanner' size distribution, based on ground-based coma observations of short-period comets (Hanner 1984), represents freshly-produced cometary material.

To determine which particles actually produce the zodiacal emission, we show the integrand from equation 1, in Figure 9. At wavelengths of strong material resonances, small particles contribute, but larger particles (10–100 μm radius) dominate the continuum, especially at long wavelengths. The size distribution is therefore a significant determinant of the strength of spectral features. For size distributions with relatively more small particles, the short-wavelength emission, as well as the spectral feature emission, can have a significant small-particle contribution, because the small particles are (for at least moderately-absorbing materials) hotter than the larger particles.

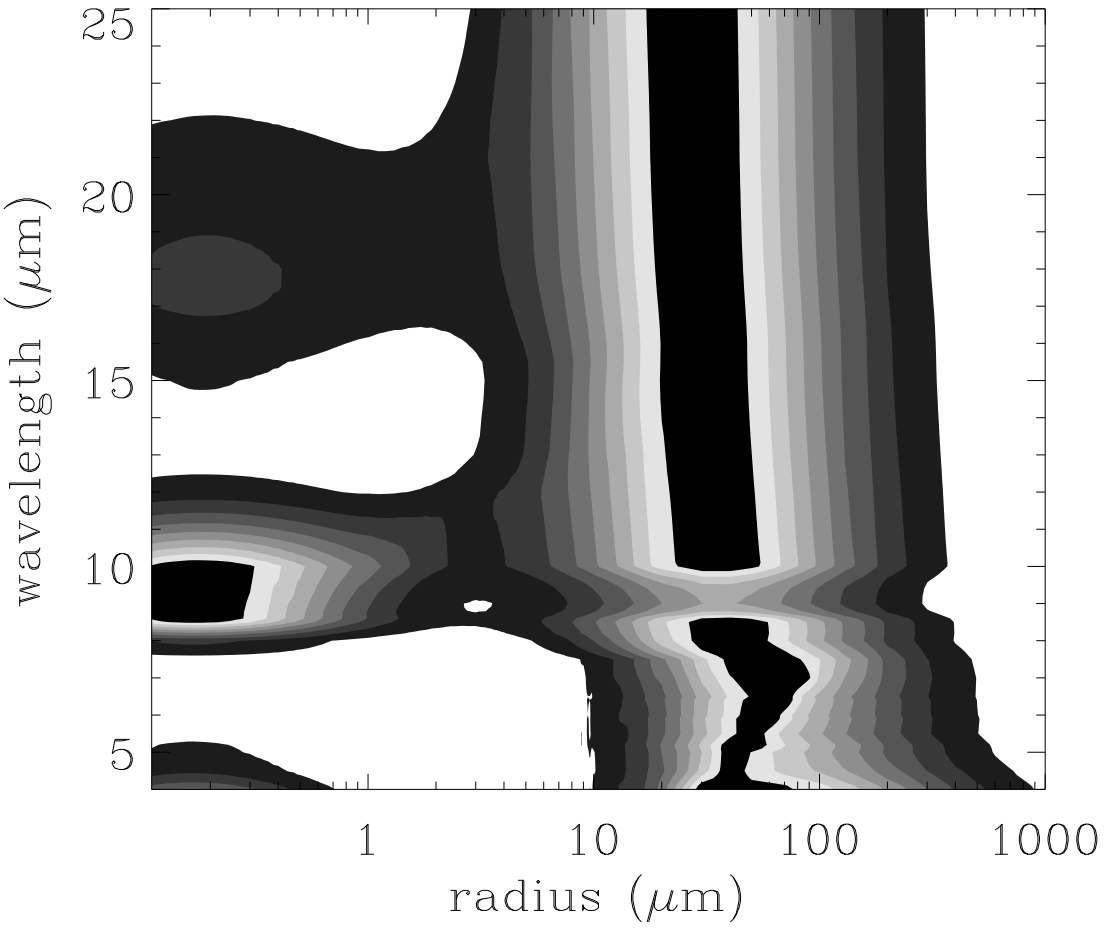

Fig. 9.— The fractional contribution of pyroxene grains of various sizes to the zodiacal light at a range of wavelengths. These data are for the amorphous pyroxene model and the interplanetary size distribution. For each wavelength, the emissivity integrand as a function of particle size (specifically, $(dn/da)B_\nu[T(a)]\pi a^2 Q_{abs}(a)a$ was normalized to its peak value. At most wavelengths, particles in the size range 10–100 μm produce the bulk of the emission. But at the wavelengths of the silicate feature, a significant proportion of the emission comes from very small particles that are not opaque at 10 μm. The rather complicated dependence of the emissivity on the particle size and wavelength makes it impossible to use single-temperature or single-size models to fit the entire spectrum.

4.4. Comparison of models to observations

Model predictions for the zodiacal spectrum are shown in Figure 10. The models can be characterized to first order as blackbody continua plus (in many cases) silicate features at 9–11 μm. Using the same fitting procedure that was used on the data, we measured the color temperature of the continuum over the ISOCAM wavelength range; Table 4 shows the results. Please note that these color temperatures are only valid over the 5–16 μm wavelength range: extrapolating these fits to longer wavelengths (*e.g.* $\lambda > 20$ μm) results in very poor predictions of the spectrum. The carbonaceous materials are generally too hot to be the dominant, individual material producing the zodiacal light. The crystalline silicates were generally too cold, but after they were 'dirtied' by adding carbonaceous material (as described above) some of their temperatures are comparable to the observed zodiacal spectra. All of the models with the Grün *et al.* (1985) interplanetary size distribution have approximately the observed color temperature, because large, opaque particles dominate the emission.

Table 4: Color temperature of model continuum[a]

	Size Distribution						
Material	hanner	power	grun	lunar	halley-la	halley-mc	halley-ks
astronomical silicate	242.2	250.0	264.2	264.9	237.6	247.7	239.5
amorphous olivine	236.1	248.6	252.1	254.9	229.6	244.5	232.9
dirty amorphous enstatite	351.9	420.2	275.1	318.8	322.0	399.8	315.4
crystalline olivine	280.6	289.5	269.3	271.9	270.6	296.1	274.1
dirty montmorillonite	372.9	446.2	273.8	325.4	336.2	432.3	328.2
glassy carbon	404.8	547.4	290.5	373.8	361.4	483.4	348.3

[a] temperature of best-fitting blackbody for wavelengths 6–16 μm excluding 8–13 μm

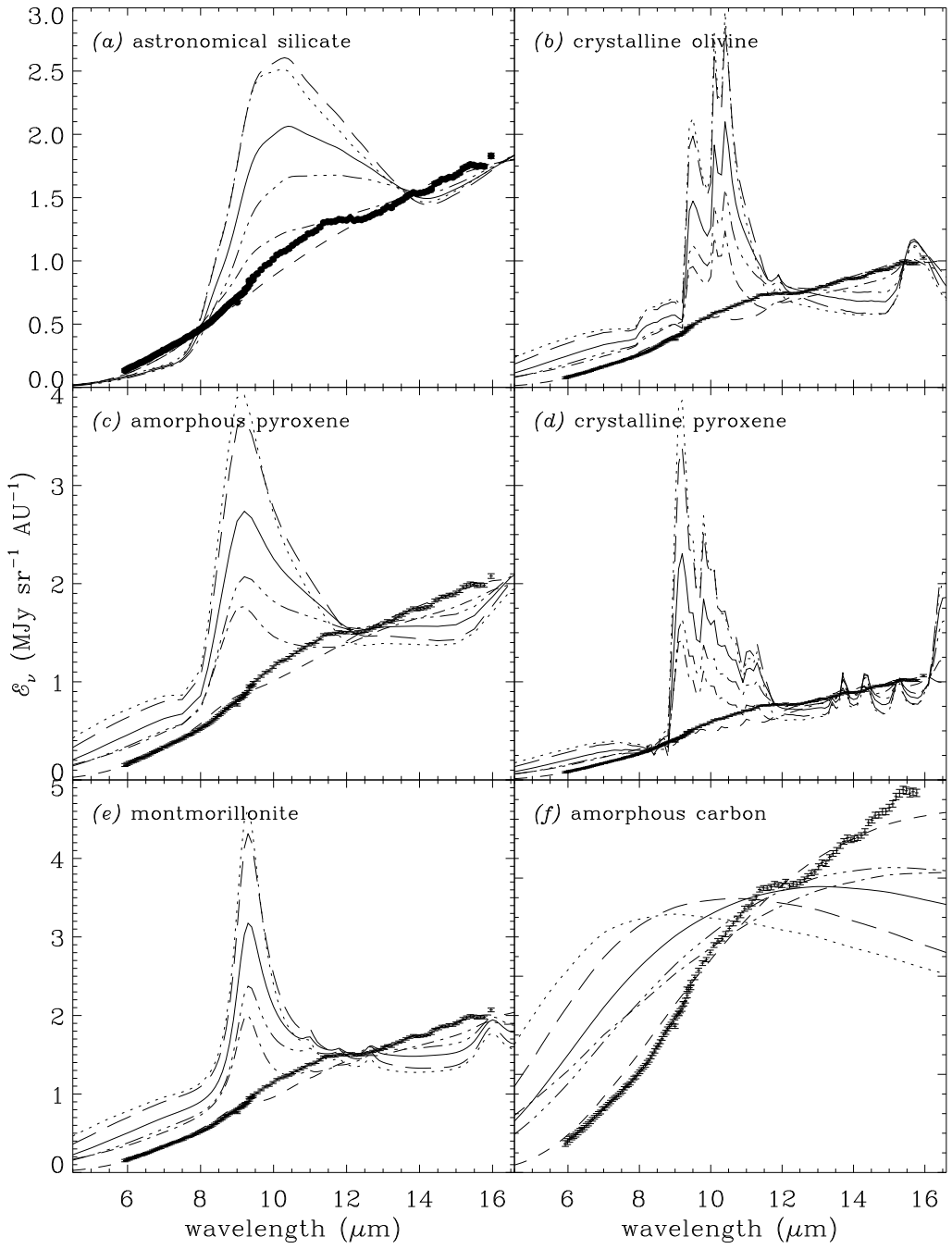

Fig. 10.— Model spectra of interplanetary dust particles at 1 AU from the Sun, for different compositions and size distributions. Each panel shows the models for one particle composition and 5 different size distributions (long dash: halley/McDonnell, dotted: interstellar, solid: Hanner, dash-dot-dot-dot: halley/Lamy, dash-dot: lunar, dashed: interplanetary; listed in order of silicate

feature strength for astronomical silicate). The 'power-law' size distribution, which has the largest abundance of small particles, has the highest-contrast spectral features, while the Grün *et al.* (1985) interplanetary size distribution, which has the lowest abundance of small particles, has essentially no silicate feature. Panel *(a)* represents interstellar material; panels *(b), (c)* represent amorphous silicates; and panel *(d)* is a crystalline silicate; panel *(e)* is a meteorite sample; and panel *(f)* is an amorphous carbon sample. In each panel, the average observed zodiacal spectrum is overplotted as a set of thick black circles. It is clear that there are no high-contrast features in the observed spectrum, ruling out essentially all of the small-particle-cominated size distributions.

The observed zodiacal spectrum has very little structure; specifically, there are no features above 10% of the continuum. In order to assess which model spectra show comparable features, we divided each model spectrum by its blackbody continuum fit (see Fig. 11). First, it is evident that all of the spectra, both model and observed, exhibit a rise at short wavelength relative to their blackbody fits. This rise can be easily explained by a range of dust temperatures contributing to the emission. The blackbody fit will yield the color temperature that dominates the 6–15 μm wavelength range. It will not include hotter dust, which dominates at shorter wavelengths because of the steepness of the Wien portion of the Planck curve. The short-wavelength rise can be due to small silicates or to carbonaceous material.

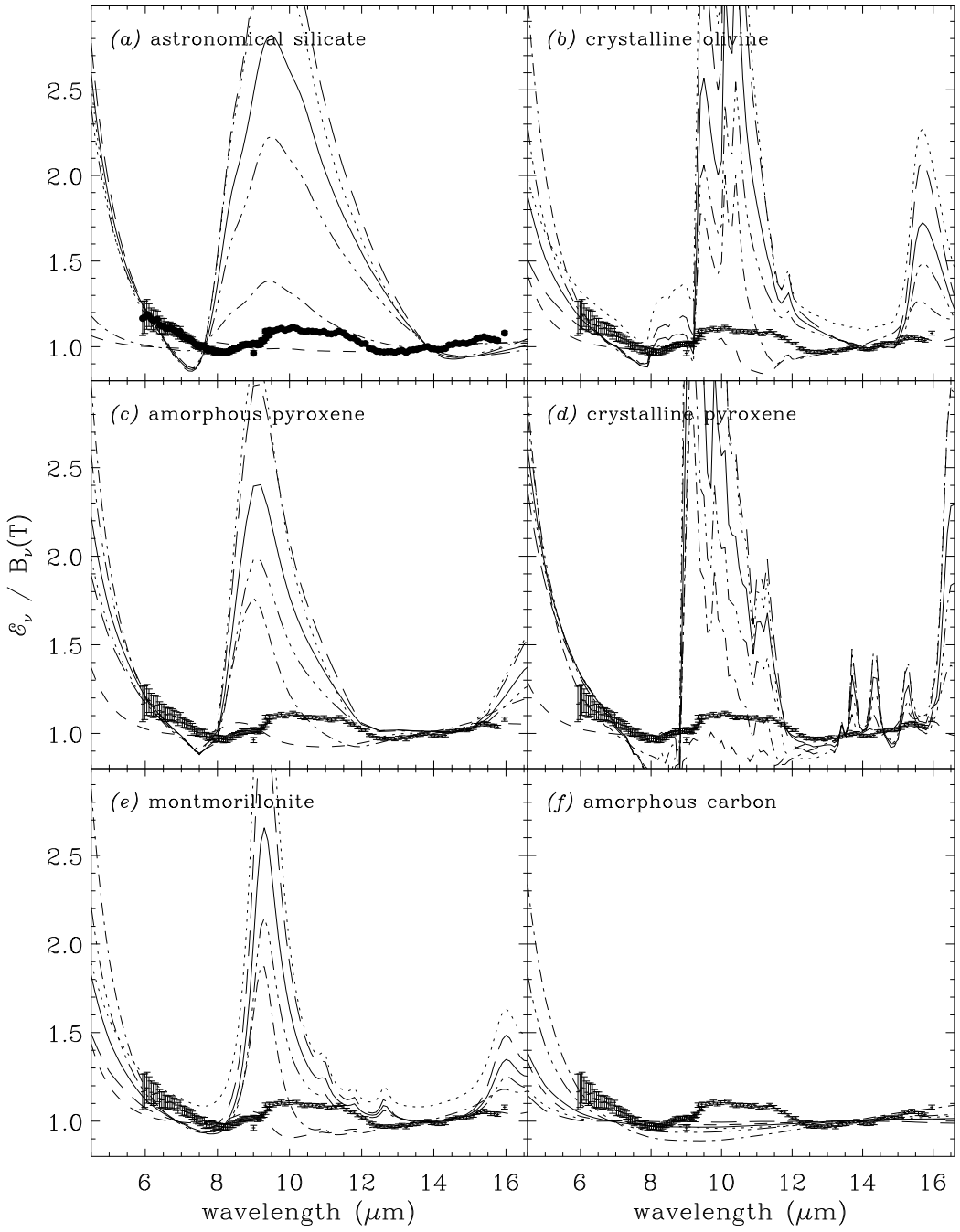

Fig. 11.— Model spectra from Fig. 10, divided by a blackbody fit to their mid-infrared continua. The fits were performed in the same way for the observed data, which are overplotted on each panel. The rise in the observed ratio spectrum at short wavelengths is reproduced in the model spectra; it is due to the spread in temperatures as a function of particle size. The bump at 9–11

μm that could be a silicate feature is roughly comparable to those predicted by the silicate models, but it does not match any of these models in detail. The zodiacal dust must include a range of different mineralogies; they cannot be dominated by a single crystalline or amorphous silicate.

The spectral features predicted by the models are generally much too strong and too structured to match the observed spectrum, except for the large-particle-dominated models. In Figure 11, it is clear that the individual silicates, both crystalline and amorphous, generate distinctive shapes in their 9–11 μm spectral features. The observed spectral feature is rather broad and smooth, lacking sharp peaks. However, the observed line is 'boxy' and the short- and long-wavelength edges of the observed feature roughly correspond to resonances in silicates. We can reach several simple conclusions from these observations. First, the short-wavelength excess emission seen in the observed spectrum is more likely due to carbonaceous (or another strongly-absorbing) material; if it were due to small, hot silicates, then the 9–11 μm feature would be much stronger. Second, the zodiacal light is produced mostly by large (> 10 μm) particles, and the size distributions with large abundances of small particles can be ruled out. From Table 5, only the interplanetary and lunar size distributions from Grün *et al.* (1985) are plausible. The other size distributions, which are based on observations of comets and the interstellar medium, all have far too many small particles, making their spectral features and too prominent (i.e. with $Delta_{sil}$ much larger than observed). Thus is is clear that zodiacal dust is very different, in size or composition, from the dust that produces the observed cometary or interstellar silicate spectral features.

Table 5: Particle size distributions[a]

Name	k_{small}	k_{large}	reference
interplanetary	-2.16	-2.00	Grün *et al.* (1985)
lunar	-3.74	-2.05	Grün *et al.* (1985)
interstellar	-3.50	-3.50	Mathis, Rumpl, and Nordsieck (1977)
Halley/Lamy	-2.53	-3.40	Lamy, Grün, and Perrin (1987)
Halley/McDonnell	-3.11	-3.96	McDonnell *et al.* (1991)
Hanner	-2.66	-3.59	Hanner (1984)

[a] k_{small} and k_{large} are the approximate power-law indices of the size distributions between particle sizes 0.3–2 μm and 2–20 μm, respectively.

4.5. Mixture model

We constructed a non-unique, but illustrative, model that quantitatively matches the broad zodiacal spectrum. The model uses a large-particle-dominated size distribution with just enough small silicates to make the weak 9–11 μm feature. A better fit to the detailed shape of the silicate feature using different particle shapes is described below; the model described here addresses the

overall spectral shape including feature and continuum. First, because the interplanetary size distribution yields no silicate features and the lunar (and other) size distributions make too strong a silicate feature, we had to construct a new size distribution. This was simply done by taking the difference between the model spectra for the interplanetary and lunar distributions, and adding in a fraction of that difference to the interplanetary distribution until it makes silicate feature amplitude comparable to the observed one. This is valid because the model is a linear function of size distribution (eq. 1), and the lunar size distribution is identical to the interplanetary size distribution except for small particles (Grün *et al.* 1985). Second, we had to combine different materials in order to generate a wide silicate feature.

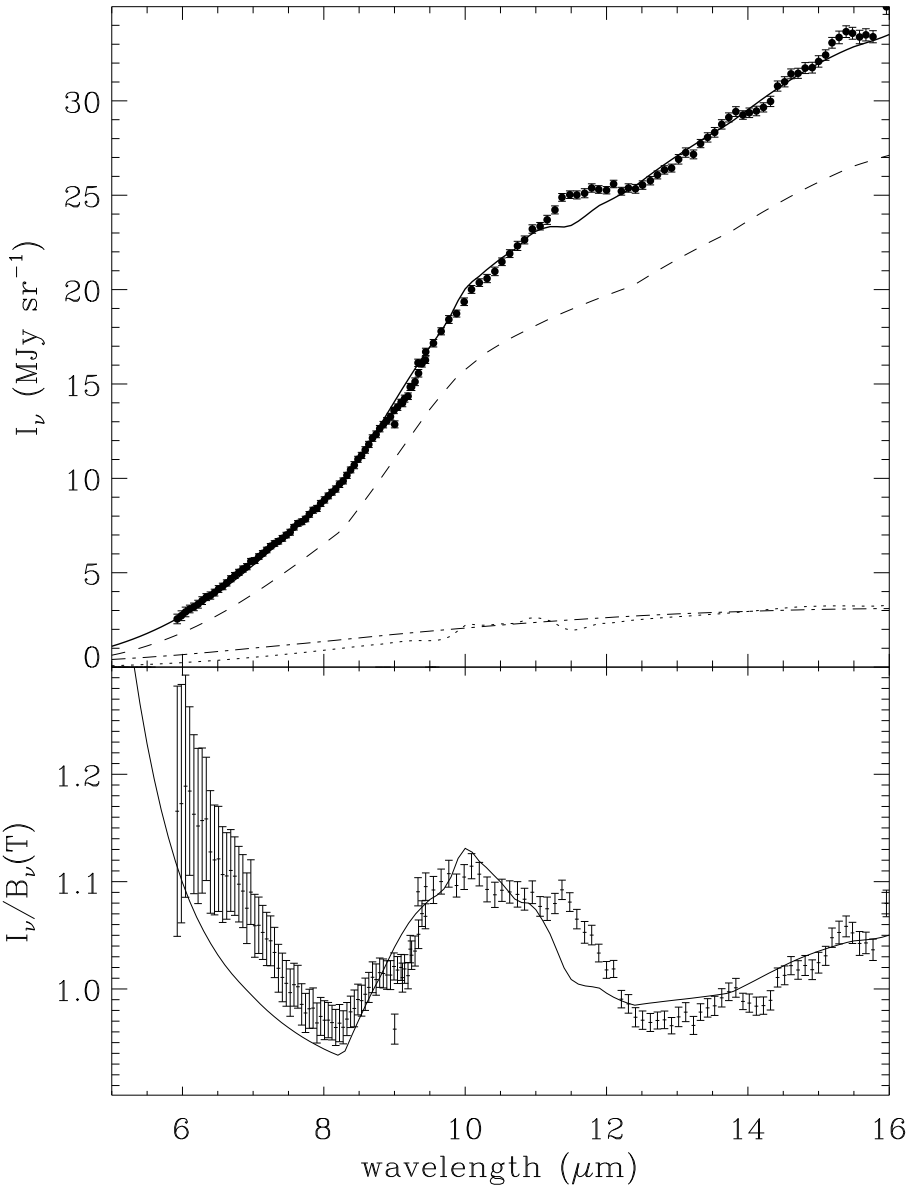

Fig. 12.— Comparison of a mix of silicates and carbonaceous materials to the observed spectrum of the zodiacal light. The top panel shows the observed spectrum (circles with error bars), together with the mixture model (solid line) and the brightness of each of the 3 components of the mixture (dash: dirty amorphous olivine, dash-dot: glassy carbon, dash: crystalline olivine). The bottom panel shows the ratio of the intensity to a blackbody continuum fit for the observed (symbols with error bars) and mixture model (line) spectra.

Figure 12 shows the mixture, compared to the observed spectrum. The fit to the spectral feature is relatively poor, but the main features of the observed spectrum are reproduced. The mixture contains three materials: amorphous forsterite/olivine from Scott and Duley (1996) [80% of the 13–15 μm intensity], crystalline olivine from Mukai and Koike (1990) [10%], and amorphous carbon from Edoh (1983) [10%]. Relative to cosmic elemental abundances, this is a silicate and oxygen-rich mixture. Most of the carbon is mixed in with the amorphous forsterite/olivine (Scott and Duley 1996), which was 'dirtied' using a 10% volume mixture of glassy carbon; the free, amorphous carbon grains contain the remaining 35% of the carbon. The relative paucity of carbonaceous material could be due to its volatility: the grains, whether originally cometary or asteroidal, have been exposed to sunlight for $> 10^6$ yr (Grün *et al.* 1985), which may be long enough to remove their volatiles. The elemental abundances from our mixture model should not be taken as the total elemental abundances of the interplanetary dust, because they are weighted toward particles that are relatively bright in the mid-infrared. The elemental abundances from our mixture model are different from those of fresh cometary ejecta, which has a significant gaseous component rich in the lighter elements (e.g. as detected by impact detectors that flew through comet Halley's coma in 1986). The size distribution is dominated by large (10–100 μm radius) particles. For crystalline olivine and amorphous carbon, the size distribution was intermediate (50% each) between the interplanetary and lunar size distributions, while the amorphous olivine, which dominates the spectrum, had a size distribution very close to interplanetary (92%, with 8% lunar).

In order to fit the detailed shape of the silicate feature, we had to consider the effect of particle *shape*. Inspecting Figure 11 carefully, it is evident that none of the theoretical models for spheres produce silicate features extending beyond 11 μm, as the observed feature does. This is true despite the presence of strong resonances in crystalline olivine at 11.4 μm (Fabian *et al.* 2001). It is a well-known property of spheres that their absorption cross-sections do not necessarily peak at the wavelengths of the resonances, instead having wavelength dependence, in the small particle approximation,

$$Q_{abs}^{sphere} = 4x\mathrm{Im}\left[\frac{\epsilon - 1}{\epsilon + 2}\right],$$

where $x = 2\pi a/\lambda$, $\epsilon = m^2$, and m is the (wavelength-dependent) complex index of refraction. This equation combines the real and imaginary parts of the index of refraction in a very specific, nonlinear way. The peaks of silicate features from spherical particles are significantly shifted from other shapes (Yanamandra-Fisher and Hanner 1999). To generalize the theoretical calculations, we fitted the shape of the silicate feature using the 'continuous distribution of ellipsoids' (CDE)

approximation, in which all possible axis ratios have equal probability; the absorption efficiency averaged over shapes is then

$$\langle Q_{abs}^{CDE} \rangle = \frac{8}{3} x \mathrm{Im} \left[\frac{\epsilon}{\epsilon - 1} \log \epsilon \right]$$

which does not shift emission features from resonances as much, though it does tend to broaden them (Bohren and Huffman 1983). This equation only applies in the small-particle limit, and the full equations for a distribution of larger ellipsoids are not known and probably computationally very challenging. Since the particles producing the continuum of zodiacal light are large (as discussed above), we cannot at present use a full theoretical CDE calculation (solving for the temperature for each particle size) for the zodiacal light. More sophisticated models of non-spherical particles, such as the discrete dipole approximation (Draine 1988) or T-matrix method (Mischenko 1991) would be able to treat the problem self-consistently, but they are far beyond the scope of this project. However, the zodiacal light silicate *feature* is produced by particles small enough that the small-particle limit can be used. Therefore, we continue to use the models for spheres, as presented in the previous sections, to calculate the continuum spectrum. To model the silicate feature, we calculated CDE absorption efficiencies for all of the materials and for 0.4 μm particle radii (see Fig. 9). A linear regression of the absorption efficiencies was fitted to the observed spectrum. If the various silicate minerals have the same size distribution, then the scale factor from the regression analysis gives the relative abundance of each mineral.

The best fit to the silicate feature includes three components; Figure 13 shows the mixture and each component. This solution was found by trying each three-way combination of 40 different theoretical models (each of the materials described above, some with and without different amounts of carbonaceous material), and identifying the solution with minimum χ^2. (Solutions with negative coefficients were discarded as nonphysical, leaving 3741 models involving combinations of various materials.) The most abundant silicate is amorphous olivine (with a scale factor of 1.12), which is the best single-mineral fit to the spectrum. However, amorphous olivine cannot fit the blue or red wing of the observed feature, which is distinctly 'boxy.' The blue wing requires a different silicate mineral, and a reasonable fit can be obtained with a hydrous silicate (montmorillonite, with a scale factor of 0.25). There is some indication of a more detailed substructure in the blue wing that can be fitted with this mineral, with a possible hump in the spectrum around 8.6 μm. None of the minerals we considered have this structure, but it is relatively subtle and uncertain so we did not pursue it further. The red wing of the zodiacal feature, including the small peak at 11.35 μm, is reasonably fit by crystalline olivine (with a scale factor of 0.12).

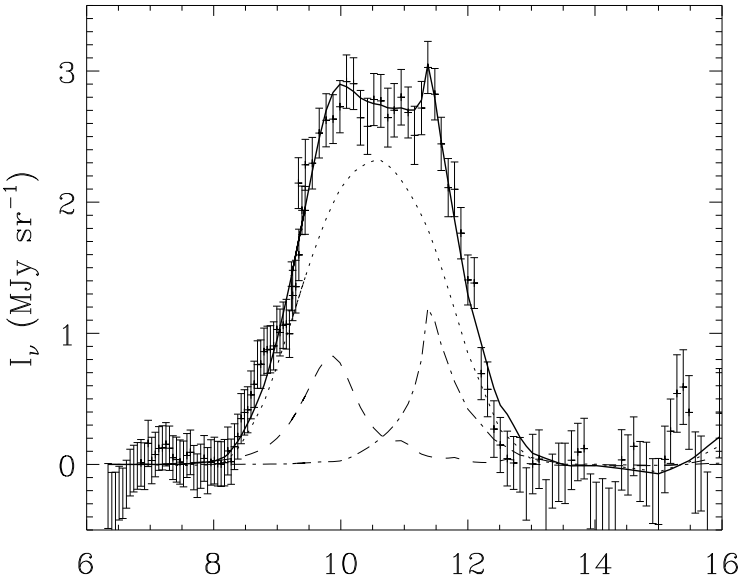

Fig. 13.— Comparison of a mixture of silicates with all possible ellipsoidal shapes to the observed, continuum-subtracted, spectrum of the zodiacal light. The solid line is the mixture fit, the dotted line is the amorphous olivine contribution, the dashed line is the montmorillonite contribution, and the dash-dotted line is the crystalline olivine contribution.

The presence of a hydrous silicate in the mixture required to fit the shape of the silicate feature indicates that the parent bodies of the zodiacal particles were formed in a location where water could be mixed with crystallizing minerals. This may suggest formation in the inner Solar System, where temperatures and pressures were high, or processing on an active surface (or in collisions). A mixture of water and minerals is certainly expected for comets, but the water is less likely to be contained so deeply within the silicate minerals. These subtle clues can reveal relationships between zodiacal particles and their parent bodies, and they need further exploration.

Using the best-fitting model, we can predict the spectrum at wavelengths outside the region we observed. Due to the prevalence of large particles, and the weakness of the 9–11 μm feature, we predict a relatively featureless spectrum. The CDE fit includes crystalline olivine, which has features at *20*, 21, *24*, and *35* μm, and montmorillonite, which has features at 19, *23*, and 29.5 μm (brightest features in *italics*). We note that earlier measurements of montmorillonite (Koike, Hasegawa, and Hattori 1982) also show a broad feature in the 45 to 55 μm range that is not reproduced in their later derivations of the optical constants (which we use here) from Lorentz oscillators. The amplitude of these features is not accurately predicted by the CDE model, because it is a single-size model. A rough estimate can be made by using the CDE mixture model to give the detailed features and the spherical model to give the continuum level. Interestingly,

the strongest crystalline olivine and hydrous silicate features alternate in wavelength, such that the sum is more like a lumpy continuum. Only the 9–11 μm feature is strong in the mixture. The next brightest features (in *italics* above) are only ~ 1 % of the continuum. Thus, apart from the 9–11 μm feature, we do not expect significant structure in the zodiacal light spectra obtained with the Infrared Spectrograph on the *Space Infrared Telescope Facility* (Houck 1995). By extension, we predict a relatively featureless spectrum for the terrestrial portion of debris disks around mature stars, where the primordial dust has been removed and the particles are derived from asteroid collisions and comet fragmentation.

5. Relation between zodiacal light and parent bodies

5.1. Comparison to IDPs and cometary dust

Sandford (1987) summarized the properties of interplanetary dust particles (IDPs) collected in the atmosphere. He divided the particles into three classes: olivines, pyroxenes, and layer-lattice silicates. All of the IDPs are heterogeneous, with the carbonaceous material that survived atmospheric entry spread throughout the grains. The collected particles are rather porous, and the 'empty' regions were probably at least partially filled with more volatile materials before atmospheric entry. These properties are consistent with our 'dirtied' silicate sphere models, although the actual porosity of the grains in space is not known and could affect the spectral properties. The infrared transmission of a sample of IDPs was measured by Sandford and Walker (1985). All of the silicates had 9–11 μm features. The olivine particles presented substructures at 9.3, 10.1, and 11.2 μm, while the pyroxenes presented substructures within the 9–11 μm band that varied strongly from particle to particle. The layer-lattice silicates have strong O–H features that would have been observable in the zodiacal spectrum. Thus, small particles composed of layer-lattice silicates are unlikely to be very abundant in interplanetary space. The observed zodiacal light spectrum, on the other hand, bears a strong resemblance to the olivine and pyroxene IDPs. The strong particle-to-particle mineralogy variations would, when blended together along the line of sight in a zodiacal light observation, lead to a relatively broad and smooth feature, which is in fact what we observe.

Comets in the inner Solar System present relatively strong 9–11 μm silicate features (Hanner, Lynch, and Russell 1994). These features vary from comet to comet, and they may be stronger for new comets. The best-observed cometary silicate feature is for comet Hale-Bopp, both because it was very bright and because of advances in infrared detection. Wooden *et al.* (1999) presented extensive ground-based observations of the 9–11 μm Hale-Bopp, and Crovisier *et al.* (1997) presented the *ISO* spectrum over a wider wavelength range. Comparing the continuum-subtracted zodiacal light and Hale-Bopp silicate features (shown together in Fig. 15 below), the amplitude of the silicate feature from the Hale-Bopp dust is twice the brightness of the underlying continuum. In our nomenclature, Δ_{sil} ranged from 160 to 200 as the Hale-Bopp moved from 2.8 to 0.9 AU

from the Sun (Wooden *et al.* 1999). Comets Halley and Mueller showed similarly strong silicate features, while comets Borrelly and Faye had weaker features, with $\Delta_{sil} \sim 20$ (Hanner, Lynch, and Russell 1994). The cometary silicate features are several to 20 times stronger than the silicate feature in the zodiacal light. For comets with infrared spectra, the particles are inferred to be much smaller than those that dominate the zodiacal light, due both to their bright silicate features and their continuum temperatures being much higher than blackbodies at the corresponding distance from the Sun. These coma grains are so small that they feel enough radiation pressure to put them in hyperbolic orbits. It is clear that these small dust grains are not the origin of interplanetary dust, unless the grains can grow in the interplanetary medium. Molster, Bradley, and Sitko (2002) suggested that some Fe-poor crystalline silicates may have condensed out of the gas phase close to the Sun, and the small grains transported by radiation pressure *over* the solar disk to distances beyond Jupiter. Larger cometary particles have been detected by *in situ* observations at P/Halley (McDonnell *et al.* 1991) and inferred by dynamic modeling of the morphology of the dust around C/Austin (Lisse *et al.* 1994) and P/Encke (Reach *et al.* 2000). Let us assume that the small cometary grains have similar mineralogy to the larger ones, so it is useful to compare the mineralogy of the cometary and zodiacal particles. First, comet grains appear to be more crystalline, with sharper substructures in their 9–11 μm feature (Wooden *et al.* 1999), and strong crystalline features in the 35 μm region (Crovisier *et al.* 1997). In Figure 15, the 11.3 μm crystalline olivine peak is clear in the Hale-Bopp silicate feature. Second, the comet grains appear to be Mg-rich (Wooden *et al.* 1999), which is similar to our results for the zodiacal light, where a forsterite material (Mg-rich olivine) matches the spectrum better than fayalite (Fe-rich). We cannot say with confidence whether there is a real distinction between what seem to be olivines (SiO_4) matching the zodiacal spectrum and the mixture of olivines and pyroxenes (SiO_3) matching the Hale-Bopp spectra (Wooden *et al.* 1999), because the zodiacal spectrum is too dominated by large particles to present clearly-defined spectral features.

5.2. Spatial variations of the zodiacal spectrum: cometary *versus* asteroidal origin for dust

A goal of this project was to determine how the zodiacal spectrum varies from place to place. To first order, the spectra are remarkably similar. The brightness is clearly higher at low ecliptic latitudes and toward the Sun, as shown in the definitive maps of the zodiacal cloud by *COBE*/DIRBE (Kelsall *et al.* 1998). For a more detailed comparison, Figure 14 shows the temperature and silicate excess determined from fits to the ISOCAM CVF spectra described earlier in this paper. The fit values are displayed in the relevant Solar System coordinate system; specifically, they are plotted as a function of angular separation from the Sun and absolute ecliptic latitude. The spectra with the lowest color temperature are those taken farthest from the Sun and at relatively lower ecliptic latitude. The warmest spectra are those closest to the Sun and at high ecliptic latitude. These variations are intuitively expected, because the sight-lines that contain the coldest dust will be those that see farthest toward the outer Solar System. The

spectra taken closest to the Sun sample the hottest dust (reaching as close as 0.9 AU). The reason the polar spectrum is among the warmest is that it contains almost exclusively dust at 1 AU, while the ecliptic plane spectrum closest to the Sun samples dust at a range of distances, from 0.9 AU outward to distances where the dust is cooler.

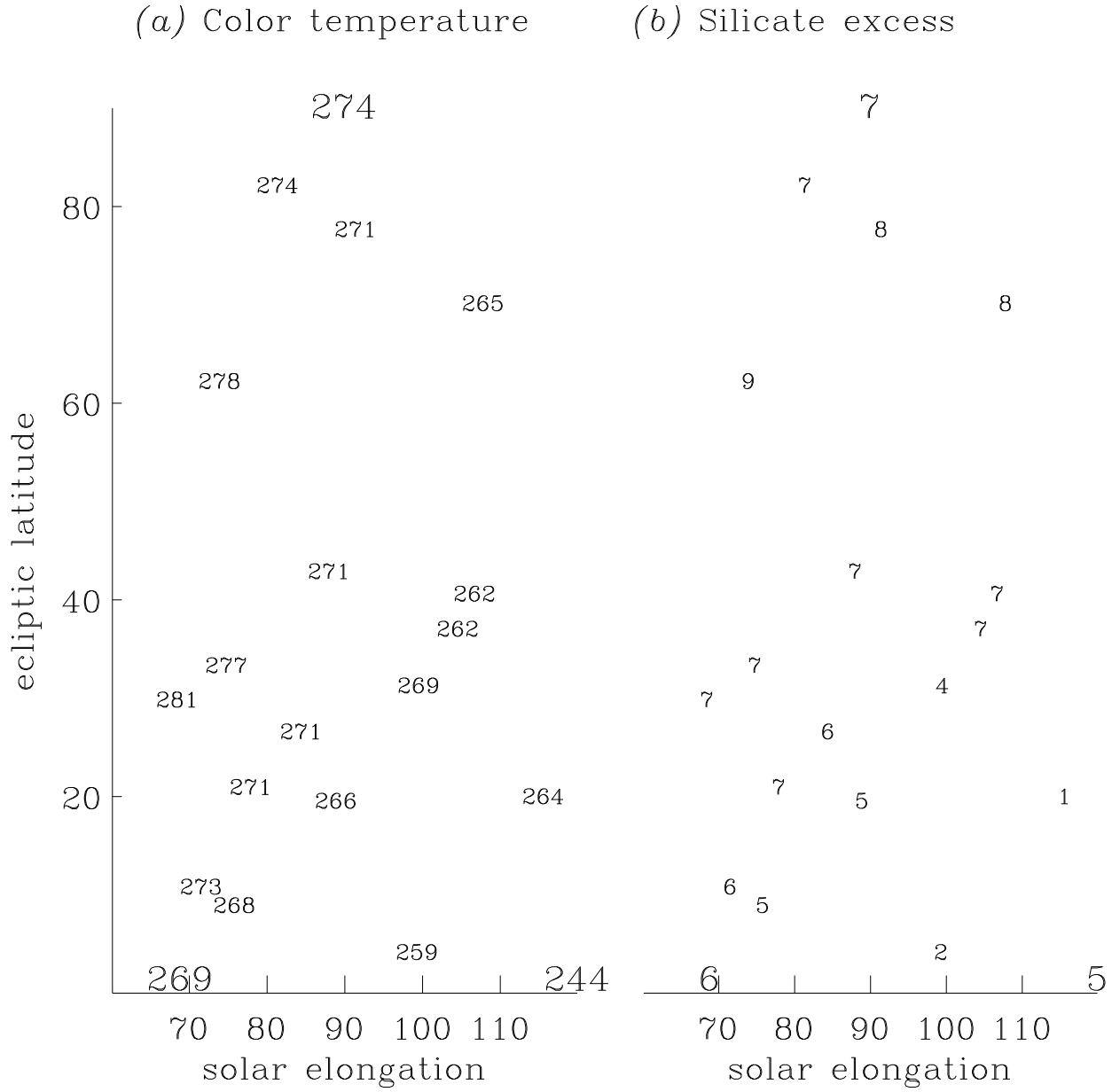

Fig. 14.— The color temperature *(a)* and silicate excess *(b)* derived from ISOCAM spectra of the zodiacal light. Both the archival and dedicated zodiacal light observations are included; the dedicated observations are distinguished by larger font.

The value of the polar temperature is very similar to the temperature (278 K) expected for rapidly-rotating, grey grains at 1 AU from the Sun. This clearly demonstrates that the spectrum is dominated by grains large enough that they emit efficiently in the mid-infrared. Specifically, $2\pi a/\lambda > 1$, where $\lambda \sim 30$ μm is the longest wavelength where the grains must emit efficiently in order to behave as greybodies. This sets a limit on the grain radii of $a > 5$ μm, consistent with the theoretical models described above, which have the emission produced by particles in the 10–100 μm size range.

The variation of the color temperature with viewing direction is qualitatively as predicted by the DIRBE zodiacal light model (Kelsall *et al.* 1998). To test this quantitatively, we evaluated a generalized version of the DIRBE zodiacal light model (§2.3.1) over the mid-infrared wavelengths at which the ISOCAM observations were made, and we used the same color-temperature-fitting routine as we used on the data. The model yields colors with approximately the same variation of temperatures with solar elongation and latitude. The pole-to-plane temperature difference at solar elongation $\epsilon = 113^\circ$ is 30 K from ISOCAM and 24 K from the DIRBE model; the in-plane ($\epsilon = 66^\circ - 113^\circ$) difference is 25 K from ISOCAM and 23 K from the DIRBE model. But the DIRBE model is consistently warmer than the ISOCAM spectra, by ~ 6 K. The discrepancy can be traced to the high dust temperature at 1 AU, $T_0 = 286$ K, used in the DIRBE model. This temperature used in the DIRBE model but was not included as a free parameter; an independent, DIRBE-based model by Wright (1998) also adopted a value of T_0, but the adopted value was $T_0 = 280$ K, which is in better agreement with the ISOCAM data.

While the continuum temperature was expected to show a reflex variation as a function of viewing direction, due to changing dust temperature as a function of distance from the Sun, the amplitude of the silicate feature, expressed as a fraction of the continuum, is expected to remain relatively constant within the inner Solar System unless the properties of the material change from place to place. In Figure 14, the silicate feature amplitude shows a possible trend as a function of viewing direction. Specifically, the feature is somewhat stronger at lower elongations and higher latitudes. This suggests that dust relatively farther from the Sun has a weaker silicate feature than dust within ~ 1.1 AU of the Sun, and possibly also dust with higher-inclination orbits has a somewhat stronger silicate feature.

The variation of the silicate feature is small, if present, which suggests that the mix of dust grains does not vary dramatically as a function of distance from the Sun or from the ecliptic. This relative uniformity applies over the range of distances within which the zodiacal light is produced. The radial range is not great: at 12 μm, in the ecliptic, toward 90° elongation, 90% of the zodiacal light is produced between the orbits of Earth and Mars (Reach 1991).

A variation in the apparent mineralogy of dust in the coma of C/Hale-Bopp was detected by Wooden *et al.* (1999), who observed the silicate feature from the comet at a range of heliocentric distances. They found that both the amplitude of the feature (relative to the continuum) and its shape varied with heliocentric distance. They inferred that there were multiple silicate

components (similar to our three-component fit to the zodiacal spectrum), and that the temperature of at least one of the components was distinct from the others. The coldest component does not become bright enough to contribute to the 9–11 μm feature until it is relatively closer to the Sun. The net effect is that the line-to-continuum ratio of the silicate feature increases as the heliocentric distance decreases. This effect goes in the same sense as the effect seen in the zodiacal light, suggesting a similar mechanism may be at play.

There have been other suggestions of variations of dust properties as a function of location in the Solar System. Renard, Levasseur-Regourd, and Dumont (1995) found that the dust albedo decreases as a function of distance from the Sun as $A \propto r^{-0.32}$. That is, they found that grains are more dark at greater distances from the Sun. This result could be qualitatively in accord with a decrease in the amplitude of the silicate feature, if the grains are larger at greater distances from the Sun, because larger grains have less silicate feature and are relatively darker. (Larger grains are more efficient at infrared absorption per unit visible absorption due to physical optics.) Whether the albedo actually varies is extremely difficult to say with confidence, and the same applies to our suggested variation in the silicate feature. From remote sensing, we only retrieve an integral along the line of sight, which cannot be uniquely inverted. The results from the *Helios* spaceprobe, which measured the brightness, color, and polarization of the zodiacal light while orbiting between 0.3 and 1 AU from the Sun, are considerably more reliable. Leinert *et al.* (1981) showed that the *Helios* results require a radial variation of the volumetric scattering cross-section $nA \propto r^{-1.3\pm0.05}$. The Kelsall *et al.* (1998) fit to the DIRBE infrared data yielded a density profile $n \propto r^{-1.34\pm.02}$ that is consistent with the volumetric scattering cross-section from *Helios*; combining these results, no variation of the albedo is required. However, the infrared model assumed constant dust properties, and it has not been determined whether a model with variable dust properties fits the data significantly better. The only convincing evidence for a variation in dust properties is the *Helios* observation that dust closer to the Sun generates relatively less polarization than dust at 1 AU (Leinert *et al.* 1981).

Radial variations in dust properties, if present, can be explained theoretically. The observations have suggested that dust is somewhat darker, more polarizing, and less silicate-feature-producing at larger distances from the Sun. Greenberg and Hage (1990) predicted varying properties of cometary dust, with relatively larger number of small grains in the inner Solar System being due to disintegration of cometary particles that consist of many small grains stuck together by volatiles, which evaporate as the grains approach the Sun. The same qualitative result is produced by grain-grain collisions, regardless of particle morphology, as very large grains, spiraling inward from the asteroid belt (for example) under the influence of Poynting-Robertson drag, are shattered by collisions before they reach the inner Solar System. Grün *et al.* (1985) calculated the collisional lifetimes to be shorter than the Poynting-Robertson lifetimes for grains larger than 100 μm. Asteroidal grains of this size would not survive into the inner Solar System.

The carriers of the silicate feature are actually very small particles. Figure 9 showed that the feature is produced most efficiently by submicron particles. Such are predicted to have very short

lifetimes, because solar radiation pressure exceeds gravity (Burns, Lamy, and Soter 1979). For the materials used in our mixture model, we calculated the ratio of radiation pressure to gravitational force, β. If the particles are compact, with volume densities $\rho \sim 2$ g cm^{-3} such as typical of terrestrial rocks and stratospheric-collected IDPs (Love, Joswiak, and Brownlee 1994), then radiation pressure exceeds gravity ($\beta > 1$) for silicate particles (both crystalline and amorphous) with radius smaller than ~ 0.4 μm. (Amorphous carbon particles always have $\beta < 1$, unless their densities are low.) If the particles are porous, then radiation pressure exceeds gravity for a proportionally larger radius, because $\beta \propto 1/(\rho a)$. Such particles should be relatively rapidly ejected from the Solar System. However, it is clear that particles of this size are present in the inner Solar System, as they were observed by dust detectors aboard Pioneers 8 and 9 and HEOS-2 (Grün *et al.* 1985). There is a continuous source of these so-called β-meteoroids, from the collisional comminution of larger particles that are spiraling toward the Sun under the influence of Poynting-Robertson drag. Thus both comets and asteroids particles can be sources of both large and small particles in the inner Solar System: Poynting-Robertson drag brings them in, and collisions grind them down.

To distinguish a cometary and asteroidal origin for the zodiacal dust, a telling variation could be a dependence of the strength (or shape) of the silicate feature on ecliptic latitude. While asteroids are confined to the ecliptic, comets have a wider range. New comets arrive at essentially all inclinations; however, nearly all of the dust they produce leaves the Solar System due to the high eccentricity of the comet's orbit and the effects of radiation pressure (Burns, Lamy, and Soter 1979). Short-period comets are the most plausible cometary source of zodiacal dust. The mean inclination of main-belt asteroid orbits is 7.9°, while the mean inclination of comet orbits is 19° (Cox 2000). Thus dust from short-period comets would be on relatively higher-inclination orbits than asteroidal dust, and it would be relatively more prevalent toward higher ecliptic latitudes.

Can we see systematic differences in the silicate feature versus ecliptic latitude? In Figure 14, there is no strong trend. The high-latitude spectra do show a silicate feature, and that feature appears to have approximately average amplitude, though perhaps on the high side. We suspect that any dependence on the orbital inclination of the parent body is masked by radial variations, so that from our vantage point near the ecliptic plane we cannot easily separate radial from vertical variations. The best chance for such a separation is to consider the spectra along the meridian where the solar elongation is 90°, and looking only at latitudes above 10°. Although the ecliptic plane will clearly contain relatively more distant dust, by moving along this meridian we will keep the mean solar distance to the emitting region at least roughly constant. We find that the high latitude points have an silicate excess $\Delta_{sil} = 7 \pm 1$, while the low-latitude points have $\Delta_{sil} = 7 \pm 1$. Thus there is no evidence for a segregation of dust properties as a function of ecliptic latitude. Our result (or non-result) is still consistent with estimates of parent sources for the interplanetary dust, which show that both comets and asteroids are viable sources. For example, Whipple (1955) predicted that short-period comets produce enough dust to maintain the zodiacal cloud, while Grogan, Dermott, and Durda (2001) showed that the asteroid families

contribute a third of the cloud and non-family asteroids can produce the rest.

6. Comparison of zodiacal and exozodiacal spectra

The new mid-infrared spectra obtained from *ISO* allow us to compare the properties of material in the interplanetary medium, comets, and in debris disks around other stars. Figure 15 compares the spectrum of the zodiacal light, comet Hale-Bopp (Crovisier *et al.* 1997), the β Pic debris disk, and the interstellar medium (Draine and Lee 1984). To make this comparison, we have subtracted smooth continua from each spectrum. The zodiacal light continuum was obtained by first removing the Kelsall *et al.* (1998) zodiacal light prediction for this line of sight and observing date. (This model uses a blackbody kernel so it will not affect the silicate feature shape). Then we subtracted a second-order polynomial in the 5–16 μm range excluding 8–12 μm. For Hale-Bopp, the continuum is simply a second-order polynomial fitted over this same wavelength range. For the interstellar spectrum, we used the theoretical model described above for astronomical silicate particles heated by the Sun at 1 AU with the interstellar size distribution (Mathis, Rumpl, and Nordsieck 1977), and then subtracted a second-order polynomial fitted over the same wavelength range as for the other spectra.

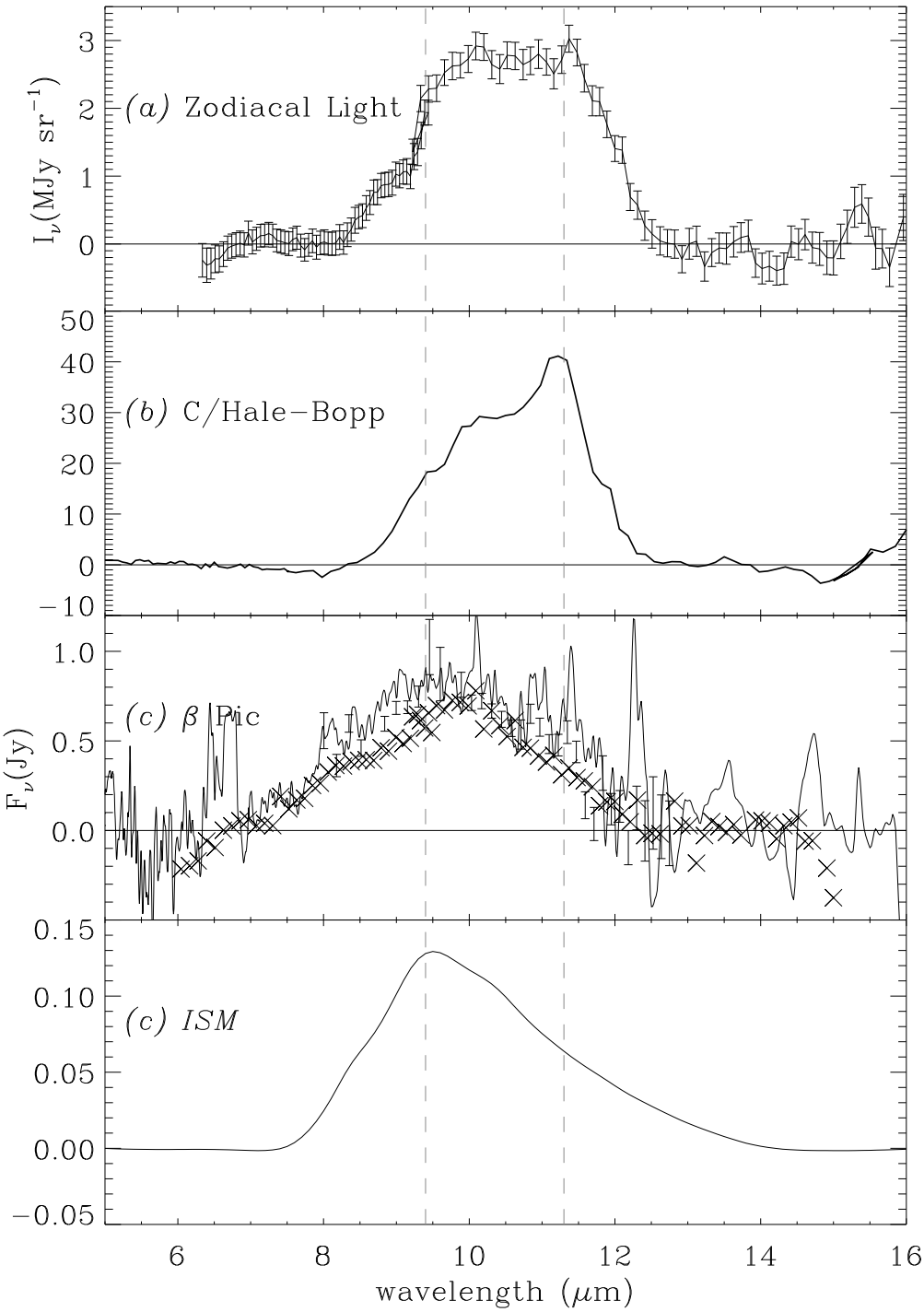

Fig. 15.— Continuum-subtracted spectra of *(a)* the zodiacal light, *(b)* comet Hale-Bopp (Crovisier *et al.* 1997), *(c)* the β Pic debris disk, and *(d)* interstellar particles (Draine and Lee 1984). The

spectra are roughly in evolutionary order, with the initial building blocks from the interstellar medium at the bottom, then the agglomerating particles in the β Pic disk, then the comet, then the cometary and asteroidal fragments of the zodiacal light. In panel *(c)*, the observed spectra (same curve and symbol coding as Fig. 5) minus the photosphere and continuum debris disk are plotted. Comparing the zodiacal and exozodiacal features, the former appears redder and relatively boxy (like the cometary spectrum), while the β Pic feature appears smoother and somewhat triangular. Vertical dashed lines are shown at two suggestive wavelengths: the 11.3 μm peak in the cometary spectrum (attributed to olivine) and the 9.4 μm peak of the interstellar astronomical silicate spectrum. (In panel *(c)*, the emission features in the 6.4–6.8 μm range are due to H_2O.)

For β Pic, the continuum was modeled using a stellar atmosphere model for the star and a simple approximation of the disk. The separation of the silicate feature and continuum is difficult for β Pic because the feature is so smooth, and there is such a wide range of physical conditions contributing along the line of sight—from the outer disk, which dominates at long wavelengths (Heinrichsen *et al.* 2000), to the inner disk, which is only revealed at mid-infrared wavelengths (Pantin, Lagage, and Artymowicz 1997) and high-resolution, coronagraphic optical images (Heap *et al.* 2000). For the large-aperture observations, which include the entire debris disk, we made a simultaneous fit to the continuum in the SWS and PHOT data (5–200 μm) using two modified blackbody components:

$$F_\nu = [(1.07 \pm 0.11) \times 10^{-5} B_\nu(77.5 \pm 1.4 \text{ K}) + (2.37 \pm 0.18 \times 10^{-8}) B_\nu(197.5 \pm 2.5 \text{ K})](12\mu\text{m}/\lambda) \quad (2)$$

where $B_\nu(T)$ is the Planck function. The two components represent the 'outer' and 'inner' exozodiacal light, respectively, with the 'outer' component being the one that dominates the far-infrared brightness and the mass of the disk. This fit, shown as a dashed line in Figure 5, becomes brighter than the photosphere at wavelengths longer than 12 μm. For the smaller aperture observations by ISOCAM, we approximated the continuum with a single blackbody component (hence the fit is only valid at wavelengths shorter than 15 μm),

$$F_\nu = 1.54 \times 10^{-9} B_\nu(300 \text{ K}), \quad (3)$$

which is shown as a dotted line in Figure 5. The continuum is weaker in the ISOCAM and ground-based mid-infrared spectra, compared to the SWS and PHOT data, because part of the 'outer' disk is resolved and excluded from the former. The comparable temperatures of the ISOCAM continuum and the 'inner' component of the SWS/PHOT continuum fit suggest they both arise from similar parts of the disk, but even the 'inner' SWS/PHOT continuum is produced from a somewhat greater distance from the star than the CAM/ground-based continuum. Recent high-angular-resolution observations with Keck by Weinberger *et al.* (2002) resolve the thermal emission from the disk even better than those described here, revealing that the spectral shape changes with distance from the star, such that the silicate feature is largely produced from the inner 1″ of the disk. A more detailed model for the debris disk is needed to study the shape of the continuum feature in detail; for our purposes, the simple models are sufficient to allow us to extract the silicate feature.

The β Pic silicate feature appears similar to that found in recently-published exozodiacal light studies. After the first detection of the silicate feature from β Pic, Telesco et al. (1991) had already noted that the silicate feature is wider than that the interstellar feature (Draine and Lee 1984). Waelkens *et al.* (1996) showed that the silicate features of β Pic and 51 Oph are very similar. van den Ancker *et al.* (2001) presented the remarkable spectrum of 51 Oph, for which the debris disk is so bright that subtraction of the central star is hardly needed in the mid-infrared. They noted the extremely wide, and somewhat triangular, shape of the silicate feature, and hypothesized that the red wing of the feature, which is wider than silicate minerals we have studied to date, may be due to a blend with a second mineral. They also found that the 51 Oph silicate feature is identical to that of symbiotic star V385 Cen but wider (on the red side) than that of Herbig Ae star AB Aur, leading to the tantalizing speculation that the dust in 51 Oph may be " 'fresh', *i.e.* recently formed rather than accreted from the interstellar medium and processed in a proto-planetary disk" (van den Ancker *et al.* 2001). Given the extreme similarity of silicate features between β Pic and 51 Oph, it is likely that the broad, triangular shape may be a characteristic feature of proto-planetary disks, and may in fact be due to processing (including agglomeration) occurring in the disk.

It is clear that the overall spectrum of the zodiacal light is very different from exozodiacal light as evidenced by β Pic or 51 Oph. These exozodiacal spectra are dominated by dust much further from their exciting stars and therefore much colder. The 10 μm silicate feature from of these disks is produced by dust in the inner disks. Thus the line-to-continuum ratio (which is a good indicator of particle size and mineralogy) is very difficult to compare: one would have to isolate the contributions form the outer and inner disk. Using the large-aperture exozodiacal spectra, we can still compare the shapes of the silicate features: the shape of the silicate feature from β Pic is quite different from that of comet Hale-Bopp, and it is somewhat different from that of the zodiacal light. While the zodiacal feature is relatively well-defined and boxy, the integrated exozodiacal feature is more broad and triangular. The cometary feature has a pronounced 11.3 μm peak, which is not present in the zodiacal or exozodiacal spectra. Silicates producing the 11.3 μm feature are likely present in both exozodiacal disks; they explain the boxy shape of the red side of the feature. In β Pic, and 51 Oph, no substructure is evident in the integrated spectrum of the entire disk, at the limit of *ISO* sensitivity. The high-angular-resolution spectra (Knacke *et al.* 1993; Weinberger *et al.* 2002) of the inner portion of the β Pic disk are actually similar to that of the zodiacal light. Any differences between the zodiacal and integrated exozodiacal may be due to different mineralogy, radiation environment, or mineralogy and temperatures contributing to the total flux. Indeed, the particle sizes and properties should be very different in the younger systems. While the younger systems retain their protoplanetary disks of dust and gas, the Solar System particles are produced by crumbling of asteroids and comets. The presence of H_2O, CO, and CO_2 disks around both 51 Oph (van den Ancker *et al.* 2001) and β Pic (Fig. 5) may lead to a significant gas-grain chemistry that changes particle properties. Also, while the young systems have very dense disks completely dominated by collisions, the Solar System is rather rarefied, and the dynamics of particles that produce the zodiacal light are dominated by Poynting-Robertson

drag.

7. Conclusions

We have presented and contrasted the mid-infrared (5–16 μm) spectra of the zodiacal light and the exozodiacal light around β Pic. These two phenomena are due to planetary systems in very different stages of evolution: while the β Pic is likely in an early, particle-agglomeration stage leading to planet formation, the Solar System is in an advanced, large-body-colliding stage. The resulting particle properties, as seen in their mid-infrared spectra, are very different. For both systems, the mid-infrared emission is due to a combination of continuum emission and a broad silicate feature. The most glaring difference between β Pic and the Solar System is the presence of significant cold dust $\gtrsim 30$ AU from β Pic that dominates the far-infrared emission and contributes significantly even in the mid-infrared. The presence of a silicate feature in both zodiacal and exozodiacal spectra clearly illustrates their differences. The zodiacal feature is weak, at only 5–7 % of the continuum, while the exozodiacal feature is brighter than the continuum. The amplitude of the silicate feature is an indicator of particle size. Theoretical models showed that the spectrum is dominated by emission from particles with radii in the range 10–100 μm. The exozodiacal feature, in contrast, is produced by smaller particles with radii smaller than $\lambda/2\pi = 2$ μm. The shape of the zodiacal silicate feature, similar to the feature seen in comets and interplanetary dust particles, spans the range 9–12 μm and is boxy. The exozodiacal (β Pic and 51 Oph) feature is broader and more triangular. Neither the zodiacal nor the exozodiacal silicate features are identical to the interstellar dust feature, which peaks on the blue side and tails off on the red side. There is a suggestive progression in the silicate feature shape as a function of evolutionary age: the initial interstellar building blocks transform into the cometary spectrum with the β Pic spectrum as an intermediate step.

This work is based on observations with ISO, an ESA project with instruments funded by ESA Member States (especially the PI countries: France, Germany, the Netherlands and the United Kingdom) with the participation of ISAS and NASA. We gratefully acknowledge help from Joris Blommaert with ISOCAM calibration issues. The search for variations in the zodiacal spectrum was inspired by Alain Léger. The research described in this paper was carried out at the California Institute of Technology under a contract with the National Aeronautics and Space Administration.

REFERENCES

Beckwith, S. V. W., T. Henning, and Y. Nakagawa 2000. Dust properties and assembly of large particles in protoplanetary disks. In *Protostars and Planets IV* (V. Mannings, A. P. Boss, and S. S. Russell, Eds.), pp. 533–558. U. Arizona Press, Tucson.

Biviano, A., J. Blommaert, O. Laurent, K. Okumura, R. Siebenmorgen, B. Altieri, O. Boulade, L. Metcalfe, & S. Ott 1998. The ISOCAM Flat Field Calibration Report, European.Space Agency

Blommaert, J. A. D. L., F. Boulanger, and K. Okumura 2001. ISOCAM CVF photometry report, ESA.technical report 2001: SAI/2001-034/Rp, ESTEC, Noorwijk.

Bohren, C. F. and D. R. Huffman 1983. *Absorption and Scattering of Light by Small Particles*. Wiley, New York.

Boulanger, F. and 16 colleagues 1996. Mid-Infrared imaging and spectroscopy in Ophiuchus. *A&A*. **315**, L325–L328.

Bradley, J. P., L. P. Keller, T. P. Snow, M. S. Hanner, G. J. Flynn, J. C. Gezo, S. J. Clemett, D. E. Brownlee, and J. E. Bowey 1999. An infrared spectral match between GEMS and interstellar grains. *Science*. **285**, 1716–1718.

Burns, J. A., P. L. Lamy, and S. Soter 1979. Radiation forces on small particles in the Solar System. *Icarus*. **40**, 1–48.

Cesarsky, C. J., A. Abergel, P. Agnese, B. Altieri, J. L. Augueres, H. Aussel, A. Biviano, J. Blommaert, J. F. Bonnal, F. Bortoletto, and 56 coauthors 1996. ISOCAM in flight. *A&A*. **315**, L32–L37.

Coulais, A. and A. Abergel 2000. Transient correction of the LW-ISOCAM data for low contrasted illumination. *Astron. Astrophs. Suppl.* **141**, 533–544.

Cox, A. N. 2000. *Allen's Astrophysical Quantities*. Springer-Verlag, New York.

Crovisier, J., K. Leech, D. Bockelee-Morvan, T. Y. Brooke, M. S. Hanner, B. Altieri, H. U. Keller, and E. Lellouch 1997. The spectrum of Comet Hale-Bopp (C/1995 01) observed with the Infrared Space Observatory at 2.9 AU from the Sun. *Science*. **275**, 1904–1907.

de Graauw, T., and 60 co-authors 1996. Observing with the ISO Short-Wavelength Spectrometer. *A&A*. **315**, L49–L54.

Demyk, K., Ph. Carrez, Ph., H. Leroux, P. Cordier, A. P. Jones, J. Borg, E. Quirico, P. I. Raynal, and L. d'Hendecourt 2001. Structural and chemical alteration of crystalline olivine under low energy He^+ irradiation. *A&A*. **368**, L38–L41.

Dermott, S. F., P. D. Nicholson, J. A. Burns, J. R. Houck 1984. Origin of the solar system dust bands discovered by IRAS. *Nature*. **312**, 505–509.

Dermott, S. F., S. Jayaraman, Y. L. Xu, B. A. S. Gustafson, J. C. Liou, J. C. 1994. A circumsolar ring of asteroidal dust in resonant lock with the Earth. *Nature*. **369**, 719–723.

Dorschner, J., B. Begemann, T. Henning, C. Jäger, and H. Mutschke 1995. Steps toward interstellar silicate mineralogy. II. Study of Mg-Fe-silicate glasses of variable composition. *A&A*. **300**, 503–520.

Draine, B. T. 1988. The discrete-dipole approximation and its application to interstellar graphite grains. *ApJ*. **333**, 848–872.

Draine, B. T. and H. M. Lee 1984. Optical properties of interstellar graphite and silicate grains. *ApJ*. **285**, 89–108.

Edoh, O. 1983. Optical Properties of Carbon from the Far Infrared to the Far Ultraviolet, Ph..D. thesis, University of Arizona

Fabian, D., T. Henning, C. Jäger, H. Mutschke, J. Dorschner, and O. Wehrhan 2001. Steps toward interstellar silicate mineralogy. VI. Dependence of crystalline olivine IR spectra on iron content and particle shape. *A&A*. **378**, 228–238.

Fajardo-Acosta, S. B. and R. F. Knacke 1995. IRAS low resolution spectra with β Pictoris-type silicate emission. *A&A*. **295**, 767–774.

Greenberg, J. M. and J. I. Hage 1990. From interstellar dust to comets – A unification of observational constrants. *ApJ*. **361**, 260–274.

Grogan, K., S. F. Dermott, and D. D. Durda 2001. The size-frequency distribution of the zodiacal cloud: Evidence from the Solar System dust bands. *Icarus*. **152**, 251–267.

Grün, E., H. A. Zook, H. Fechtig, and R. H. Giese 1985. Collisional balance of the meteoritic complex. *Icarus*. **62**, 244–272.

Grün, E., and 23 colleagues 2001. Broadband infrared photometry of comet Hale-Bopp with ISOPHOT. *A&A*. **377**, 1098–1118.

Hanner, M. S. 1984. A comparison of the dust properties in recent periodic comets. *Adv. Space Res.*. **4.9**, 189–196.

Hanner, M. S., D. K. Lynch, and R. W. Russell 1994. The 8–13 micron spectra of comets and the composition of silicate grains. *ApJ*. **425**, 274–285.

Hayward, T. L., M. S. Hanner, and Z. Sekanina 2000. Thermal Infrared Imaging and Spectroscopy of Comet Hale-Bopp (C/1995 O1). *ApJ*. **538**, 428–455.

Heap, S. R.. D. J. Lindler, T. M. Lanz, M., R. H. Cornett, I. Hubeny, S. P. Maran, and B. Woodgate 2000. Space Telescope Imaging Spectrograph Coronagraphic Observations of β Pic. *ApJ.* **539**, 435–444.

Heinrichsen, I., H. J. Walker, U. Klaas, U., R. J. Sylvester, and D. Lemke, D. 1999. An infrared image of the dust disc around beta PIC. *MNRAS.* **304**, 589–594.

Houck, J. R. and J. E. Van Cleve 1995. IRS: an infrared spectrograph for SIRTF. *Proc. Soc. Photo-Opt. Inst. Eng.* **2475**, 456–463.

Jäger, C., F. J. Molster, J. Dorschner, Th. Henning, H. Mutschke, and L. B. F. M. Waters 1998. Steps toward interstellar silicate mineralogy. IV. The crystalline revolution. *A&A.* **339**, 904–916.

Kelsall, T., J. L. Weiland, B. A. Franz, W. T. Reach, R. G. Arendt, E. Dwek, H. T. Freudenreich, M. G. Hauser, S. H. Moseley, N. P. Odegard, R. F. Silverberg, and E. L. Wright 1998. The COBE Diffuse Infrared Background Experiment search for the cosmic infrared background. II. Model of the interplanetary dust cloud. *ApJ.* **508**, 44–73.

Kessler, M. F., J. A. Steinz, M. E. Anderegg, J. Clavel, G. Drechsel, P. Estaria, J. Faelker, J. R. Riedinger, A. Robson, B. G. Taylor, S. Ximenez de Ferran 1996. The Infrared Space Observatory (ISO) mission. *A&A.* **315**, L27–L31.

Knacke, R. F., S. B. Fajardo-Acosta, C. M. Telesco, J. A. Hackwell, D. K. Lynch, and R. W. Russell 1993. The Silicates in the Disk of beta Pictoris. *ApJ.* **418**, 440–450.

Koike, C., and S. Hiroshi 1990. Optical Constants of Hydrous Silicates from 7 μm to 400 μm. *MNRAS.* **246**, 332–336.

Koike, C., H. Hasegawa, and T. Hattori 1982. Mid- and far-infrared extinction coefficients of hydrous silicate minerals. *Ap&SS.* **88**, 89–98.

Lagage, P.-O., O. Boulade, C. J. Cesarsky, T. Douvion, V. Mannings, E. Pantin, and A. Sargent 1999. ISOCAM spectro-imaging observations of the β-Pictoris dust disk. In *The Universe as seen by ISO* (P. Cox and M. F. Kessler, Eds.), pp. 207–210. ESA, Noordwijk.

Lamy, P. L., E. Grün, and J. M. Perrin 1987. Comet P/Halley–implications of the mass distribution function for the photopolarimetric properties of the dust coma. *A&A.* **187**, 767–773.

Landgraf, M., W. J. Baggaley, E. Grün, H. Krüger, and G. Linkert 2000. Aspects of the mass distribution of interstellar grains in the Solar System from in-site measurements. *J. Geophys. Res..* **105**, 10343–10352.

Laor, A. and B. T. Draine 1993. Spectroscopic constraints on the properties of dust in active galactic nuclei. *ApJ.* **402**, 441–468.

Leinert, C., I. Richter, E. Pitz, and B. Planck 1981. The zodiacal light from 1.0 to 0.3 AU as observed by the Helios space probes. *A&A.* **103**, 177–188.

Lisse, C. M., H. T. Freudenreich, M. G. Hauser, T. Kelsall, S. H. Moseley, W. T. Reach, and R. Silverberg 1994. Infrared Observations of Comet Austin (1990V) by the COBE/Diffuse Infrared Background Experiment. *ApJ.* **432**, L71–L74.

Love, S. G., D. J. Joswiak, and D. E. Brownlee 1994. Densities of stratospheric micrometeorites. *Icarus.* **111**, 227–236.

Malfait, K., C. Waelkens, J. Bouwman, A. de Koter, and L. B. F. M. Waters 1999. The ISO spectrum of the young star HD 142527. *A&A.* **345**, 181–186.

Mathis, J. S., W. Rumpl, and K. H. Nordsieck 1977. The size distribution of interstellar grains. *ApJ.* **217**, 425–433.

McDonnell, J. A. M., P. L. Lamy, and G. S. Pankiewicz 1991. Physical properties of cometary dust. In *Comets in the post-Halley era* (R. L. Newburn, Jr., M. Neugebauer, and J. Rahe, Eds.), pp. 1043–1073. Kluwer, Dordrecht.

McDonnell, J. A. M. and D. J. Gardner 1998. Meteoroid morphology and densities: decoding satellite impact data. *Icarus.* **133**, 25–35.

Meeus, G., L. B. F. M. Waters, J. Bouwman, M. E. van den Ancker, C. Waelkens, and K. Malfait 2001. ISO spectroscopy of circumstellar dust in 14 Herbig Ae/Be systems: Towards an understanding of dust processing. *A&A.* **365**, 476–490.

Mischenko, M. I. 1991. Extinction and polarization of transmitted light by partially aligned nonspherical grains. *ApJ.* **367**, 561-574.

Molster, F. J., J. P. Bradley, and M. L. Sitko 2002. The Origin of the Crystalline Silicates in our Solar System. *Lunar Planet. Sci.* **XXXIII**, 33;1471.

Mukai, T., and C. Koike 1990. Optical constants of olivine particles between wavelengths of 7 and 200 microns. *Icarus.* **87**, 180–187.

Okumura, K. 2001. Optical properties of ISOCAM and/or ISO telescope. In *The Calibration Legacy of the ISO mission (ESA SP-481)* (ESA, Eds.), pp. 48. ESA, Noorwijk.

Ootsubo, T. 2002. Study on interplanetary dust based on the mid-infrared observation of zodiacal emission by the IRTS, Thesis,.University of Tokyo.

Ootsubo, T., T. Onaka, I. Yamamura, T. Tanabé, T. L. Roellig, L.-W. Chan, and T. Matsumoto 1998. IRTS observation of the mid-infrared spectrum of the zodiacal emission. *Earth Planets Space*. **50**, 507–511.

Pantin, E., P.-O. Lagage, and P. Artymowicz 1997. Mid-infrared images and models of the beta Pictoris dust disk. *A&A*. **327**, 1123–1136.

Pantin, E., C. Waelkens, and K. Malfait 1999. SWS observations of the β Pictoris dust disk. In *The Universe as seen by ISO* (P. Cox and M. F. Kessler, Eds.), pp. 385–388. ESA, Noordwijk.

Preibisch, Th., V. Ossenkopf, H. W. York, and Th. Henning 1993. The influence of ice-coated grains on protostellar spectra. *A&A*. **279**, 577–588.

Reach, W. T. 1988. Zodiacal emission. I - Dust near the earth's orbit. *ApJ*. **335**, 468–485.

Reach, W. T. 1991. Zodiacal Emission. II. Dust near ecliptic. *ApJ*. **369**, 529–543.

Reach, W. T. 2000. SIRTF background estimation: methods and implementation, SIRTF Science Center Memo (http://sirtf.caltech.edu/SSC/C_PropKit/bgdoc_release.pdf): Caltech, Pasadena.

Reach, W. T., B. A. Franz, J. L. Weiland, M. G. Hauser, T. N. Kelsall, E. L. Wright, G. Rawley, S. W. Stemwedel, W. J. Spiesman 1995. Observational Confirmation of a Circumsolar Dust Ring by the COBE Satellite. *Nature*. **374**, 521–523.

Reach, W. T. and 12 colleagues 1996. Mid-Infrared spectrum of the zodiacal light.. *A&A*. **315**, L381–L384.

Reach, W. T., B. A. Franz, J. L. Weiland 1997. The Three-Dimensional Structure of the Zodiacal Dust Bands. *Icarus*. **127**, 461–484.

Reach, W. T., W. F. Wall, and N. Odegard 1998. Infrared excess and molecular clouds: a comparison of new surveys of far-infrared and H I 21 centimeter emission at high galactic latitudes. *ApJ*. **507**, 507–525.

Reach, W. T., M. V. Sykes, D. Lien, and J. K. Davies 2000. The Formation of Encke Meteoroids and Dust Trail. *Icarus*. **148**, 80–94.

Renard, J. B., A. C. Levasseur-Regourd, and R. Dumont 1995. Properties of interplanetary dust from infrared and optical observations. II. Brightness, polarization, temperature, albedo and their dependence on elevation above the ecliptic. *A&A*. **304**, 602–609.

Sandford, S. A. 1987. The collection and analysis of extraterrestrial dust particles. *Fund. Cosmic Phys.*. **12**, 1–73.

Sandford, S. A. and R. M. Walker 1985. Laboratory infrared transmission spectra of individual interplanetary dust particles from 2.5 to 25 microns. *ApJ.* **291**, 838–851.

Scott, A. and W. W. Duley 1996. Ultraviolet and Infrared Refractive Indices of Amorphous Silicates. *ApJS.* **105**, 401–405.

Telesco, C. M., and R. F. Knacke 1991. Detection of silicates in the Beta Pictoris disk. *ApJ.* **372**, L29.

Tran, Q. D. and 12 colleagues 2001. ISOCAM-CVF 5–12 micron spectroscopy of ultraluminous infrared galaxies. *ApJ.* **552**, 527–543.

van den Ancker, M. E., G. Meeus, J. Cami, L. B. F. M. Waters, and C. Waelkens 2001. The composition of circumstellar gas and dust in 51 Oph. *A&A.* **369**, L17–L21.

Waelkens, C., and 20 coauthors 1996. SWS observations of young main-sequence stars with dusty circumstellar disks. *A&A.* **315**, L245–L248.

Weinberger, A. J., E. E. Becklin, and B. Zuckerman 2002. Spatially resolved infrared imaging and spectroscopy of β Pictoris. *ApJ.* , in preparation.

Whipple, F. L. 1955. A comet model. III. The zodiacal light. *ApJ.* **121**, 750–770.

Wooden, D. H., D. E. Harker, C. E. Woodward, H. M. Butner, C. Koike, F. C. Witteborn, and C. W. McCurtry 1999. Silicate mineralogy of the dust in the inner coma of comet C/1995 O1 (Hale-Bopp) pre- and post-perihelion. *ApJ.* **517**, 1034–1058.

Wright, E. L. 1998. Angular Power Spectra of the COBE DIRBE Maps. *ApJ.* **496**, 1–8.

Yanamandra-Fisher, P. A., and M. S. Hanner 1999. Optical Properties of Nonspherical Particles of Size Comparable to the Wavelength of Light: Application to Comet Dust. *Icarus.* **138**, 107–128.